IOPscience iopscience.iop.org

Home Search Collections Journals About Contact us My IOPscience

Coherence and spin effects in quantum dots

This article has been downloaded from IOPscience. Please scroll down to see the full text article.

2007 J. Phys.: Condens. Matter 19 233201

(http://iopscience.iop.org/0953-8984/19/23/233201)

View the table of contents for this issue, or go to the journal homepage for more

Download details:
IP Address: 129.252.86.83
The article was downloaded on 28/05/2010 at 19:09

Please note that terms and conditions apply.

IOP PUBLISHING JOURNAL OF PHYSICS: CONDENSED MATTER

J. Phys.: Condens. Matter **19** (2007) 233201 (35pp) doi:10.1088/0953-8984/19/23/233201

TOPICAL REVIEW

Coherence and spin effects in quantum dots

S Katsumoto

Institute for Solid State Physics, University of Tokyo, 5-1-5 Kashiwanoha, Kashiwa, Chiba 277-8581, Japan

E-mail: kats@issp.u-tokyo.ac.jp

Received 16 November 2006, in final form 14 March 2007
Published 8 May 2007
Online at stacks.iop.org/JPhysCM/19/233201

Abstract

This review focuses on experiments on coherent transport through quantum dot systems. The most important quantity obtained in coherent transport is the phase shift through the dots, which gives complementary information to the scattering amplitude (i.e. the conductance). However, two-terminal devices have a particular difficulty, called 'phase rigidity', in obtaining the phase shift. There are two representative ways to avoid this problem: one is to adopt a multi-terminal configuration and another is to use resonance in the interferometer. This review mainly reviews the latter approaches. Such resonance in the whole interferometer often joins with local resonance inside the interferometer and appears as the Fano effect, which is a powerful tool for investigating the phase shift problem with the aid of theories. In addition to such resonances of single-electron states, electron spin causes a kind of many-body resonance, that is, the Kondo effect. Combination of these resonances is the Fano–Kondo effect. Experiments on the Fano–Kondo effect, which unveil the nature of the Kondo resonance, are also reviewed.

(Some figures in this article are in colour only in the electronic version)

Contents

 © 2007 IOP Publishing Ltd Printed in the UK

1. Introduction

A semiconductor quantum dot (QD) is often referred as an 'artificial atom' [1, 2] because of the freedom in designing the confinement potential and the *in situ* controllability of the parameters. Coherent transport through a QD can be viewed as a scattering experiment [3], in which the phase shift is as important as the scattering amplitude. The latter corresponds to the conductivity of the device while the former can be measured through interference. As noted in [4], information about the phase shift should be included in the lineshape of the conductivity against the energy of incident electrons, i.e. the gate voltage of the dot in the conventional experimental set-up. However, in real experimental situations it is not easy to measure the conductance lineshapes versus the gate voltage in a wide range without changing the dot parameters. Hence measurement of the phase shift through interference and measurement of the scattering amplitude (i.e. the conductance) constitute complementary information.

Figure 1 displays the four representative lineshapes of Coulomb oscillation treated in this article. The number of electrons N in the dot changes one by one when the gate voltage that shifts the electrostatic potential of the dot and the Fermi level in the leads, attached via tunnel junctions, passes through a resonant energy level in the dot at a boundary of N. In an ordinary Coulomb oscillation (figure 1(a)) the conductance forms peaks (Coulomb peaks) at such boundaries due to the fluctuation of electron number in the QD. At the same time the phase shift through the dot varies sharply at the resonances by π. When a dot is placed in an electron interferometer, as illustrated in figure 1(b), this results in a sharp transition of the interference from destructive to constructive, or vice versa, causing large distortion in the peak lineshape, which is called the Fano effect (see section 3.2). Many-body interaction between a localized electron spin in the dot and those of surrounding conduction electrons, which results in the Kondo effect, modifies the lineshape largely as shown in figure 1(c). Since the spin-1/2 ($SU(2)$) Kondo effect causes locking of the phase shift to $\pi/2$, reflecting its many-body resonance nature, the interference (or resonance) of the Kondo singlet state results in a peculiar transmission lineshape illustrated in figure 1(d), i.e. the Fano–Kondo effect.

The first two lineshapes come from essentially single-electron resonance. In many cases electron interferometers resemble those for microwaves composed of closed waveguides, in that electrons do not escape through potential barriers defining the electron circuits. This property causes multiple reflection from an interferometer to a dot under measurement. In the extreme of strong reaction from an outer interference circuit (strong coupling limit), we should treat

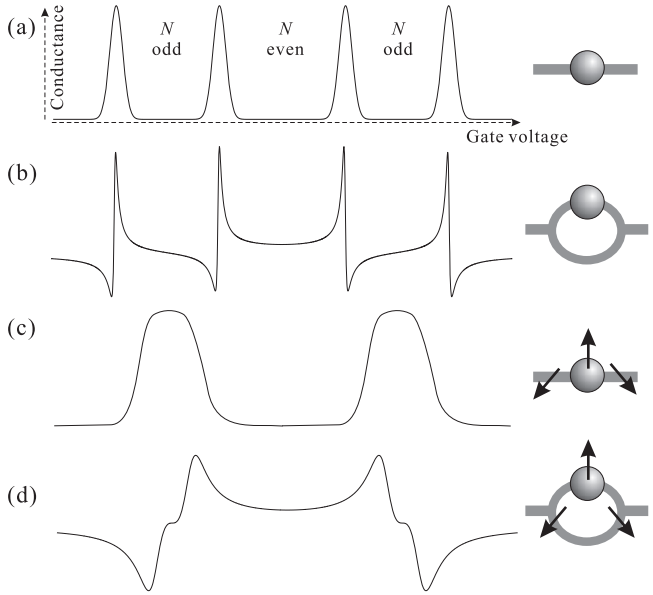

Figure 1. Schematic diagrams of Coulomb oscillation in a quantum dot for zero source–drain bias under various conditions. The corresponding configuration of the leads is displayed on the right. (a) Ordinary Coulomb oscillation in a QD with a source and a drain. The number of electrons N in the dot changes one by one with the gate voltage and the conductance has maxima (Coulomb peaks) at the boundaries of different N. (b) When a QD is embedded in a 'closed' interferometer, the Coulomb peaks become distorted due to the Fano effect. (c) When a QD has an isolated spin and the Kondo effect comes into play, the conductance at Coulomb valleys is enhanced and two adjacent peaks merge into one in the unitary limit. (d) The Kondo cloud around the QD shows peculiar interference effect called the Fano–Kondo effect, exhibiting plateau structures due to phase shift locking.

the whole system as a resonator having a QD inside. In such a situation of 'indistinguishable sample and leads', there is interplay between the dot and the interferometer. Such system can then be viewed as an 'artificial atomic system' rather than a single artificial atom and the total transmission itself is of interest.

On the other hand, the last two lineshapes have been closely related to indirect interaction between conduction electrons through spin-scattering at the QDs. A QD with an odd number of electrons inevitably has a localized spin ($1/2$ in the simplest model) on it. The local spin introduces a many-body nature into the transport over the dot via spin scattering, the Kondo effect, etc. The phase shift measurement gives important information for the investigation of such phenomena, and in the strong coupling limit novel complex phenomena of quantum interference and spin-related many-body effects are expected.

All the four interferometers illustrated in figure 1 are two-terminal devices, that is, each of them has a single inlet and outlet. A representative electron interferometer is the Aharonov–Bohm interferometer (ABI) in figure 1(b). However, as we will see in the next section, two-terminal ABIs have a serious problem called 'phase rigidity' in which the phase shift of the Aharonov–Bohm oscillation in the conductance is locked to 0 or π (see section 2.1). A way to overcome this difficulty is to adopt a multi-terminal configuration. The Weizmann group is the world leader in experiments on this. Much important knowledge has been obtained from their work, which is reviewed and analysed in many publications [5]. Another way is to analyse

detailed lineshapes of the Coulomb peaks in two-terminal devices and to deduce the phase shift with the aid of theories based on appropriate models.

In this review we consider experiments using the latter method, which were mainly carried out by a group at Tokyo University. First we pay attention to the appearance of the single electron interference effect in QD circuits, then go into many-body effects with emphasis on the effect of spins on it, above all the Kondo effect.

2. Interference circuits with quantum dots

2.1. Phase tuning and interferometers

For interferometry we need to tune the phase of the electron wavefunctions with some external parameters. Two representative parameters are magnetic field and electric field. The former is controlled simply by applying an external magnetic field, thus modifying the phase through the Aharonov–Bohm effect [6], while the latter is usually applied locally by using lithographically fabricated metallic gates which modulate the phase through the variation in the Fermi wavelength, as we see in the following.

Aharonov–Bohm (AB) phase tuning is the most popular method for phase tuning in electron interferometers. In the presence of a vector potential $\boldsymbol{A}$, an electron gains an additional phase (AB phase)

$$\theta_{\mathrm{AB}} = \frac{e}{\hbar}\int_1^2 \boldsymbol{A}\cdot \mathrm{d}\boldsymbol{s}, \tag{1}$$

when it traverses from point 1 to 2, where $\mathrm{d}\boldsymbol{s}$ is a line element on the path. θ_{AB} is tunable through the magnetic field and as easily guessed from (1) is independent of the kinetic energy or other electron parameters. In other words, the AB phase is a kind of Berry phase [7] and only depends on the path geometry and the vector potential. This makes the situation extremely simple.

The gate voltage V_{W} applied to the path of the electrons, i.e. the electric field to the electron, is another candidate. The shift of the kinetic energy $(\hbar k)^2/2m^*$ compensates the potential energy eV_{W} resulting in the shift of the wavevector; hence the phase shift at the Fermi wavevector k_{F} in a one-dimensional model is

$$\theta_{\mathrm{EL}} = \int_1^2 \left(\frac{\sqrt{2m^*(E_{\mathrm{F}} - eV_{\mathrm{W}})}}{\hbar} - k_{\mathrm{F}} \right) \mathrm{d}l, \tag{2}$$

where $\mathrm{d}l$ is a line element on the path from point 1 to 2. θ_{EL} depends on k_{F} and m^* (E_{F}). Equation (2) gives different values for different conductance channels from that in k_{F}, and this method is only applicable for single-channel conduction except for cases in which we have effective way to resolve the contribution of a single channel to the total conductance (see section 3.3).

After the selection of the phase tuning method, we need to make an interferometer that has a QD in an interference path. A simple interferometer comprises a fork, a path under measurement, another path for reference and a junction. The interference pattern is obtained from the output by tuning the path length or the phase shift through the reference path. Figure 2 summarizes the two-terminal electron interferometers with a QD which appear in this review. Regarding the spatial structure, figure 2(a) is the most complicated and (c) the simplest, though conceptually (a) is the simplest and some hidden interference paths exist in (b) and (c).

Figure 2(a) depicts a ring type interferometer with two wires, for which AB phase tuning is most frequently used. This configuration is thus called an Aharonov–Bohm interferometer (ABI). The difference between the AB phases of the two paths is given as $2\pi\phi/\phi_0$, where ϕ is

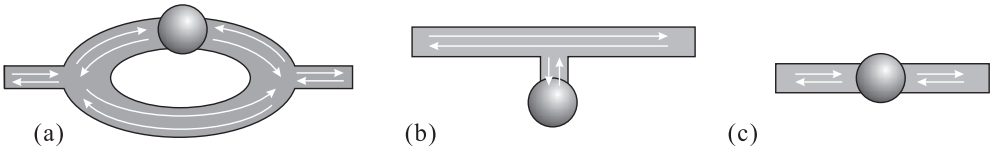

Figure 2. Schematic diagrams of various interferometers with quantum dots. White arrows indicate the directions of electron wave propagation. (a) Aharonov–Bohm (AB) ring with a quantum dot. (b) T-shaped interferometer or stub resonator with a quantum dot at the end of the stub. (c) Single quantum dot circuit.

the magnetic flux piercing the area encircled by the paths and $\phi_0 \equiv h/e$ is the flux quantum. The interference pattern is then given as

$$\rho_{2t}(\phi) \propto \cos\left(2\pi \frac{\phi}{\phi_0} + \theta_{\text{off}}\right), \tag{3}$$

where the offset phase θ_{off} contains the system information in the case of a double-slit like open interferometer. However, Onsager reciprocity requires [8] a two-terminal resistance ρ_{2t} to be symmetric for magnetic field B, namely,

$$\rho_{2t}(B) = \rho_{2t}(-B). \tag{4}$$

Equations (3) and (4) require θ_{off} to be 0 or ϕ. This is called 'phase rigidity', and is a serious obstacle to phase measurement.

Phase rigidity in a two-terminal ABI comes from unitarity of the device, i.e. the conservation of the total probability amplitude. In Young's double slit experiment, only the probability current along the detection angle contributes to the signal and the other part is lost. On the other hand the component that does not transmit through a two-terminal device should be reflected to the source. Hence a way to avoid the problem is to throw away the component that does not go into the detector (i.e. the output line) in the first passing process. Schuster *et al* [13] first demonstrated that phase rigidity can be broken by adopting a multi-terminal configuration.

Another way to express the origin of phase rigidity is by multiple reflections of the waves at the crossing points in the interferometers. Multiple reflections at the same time add a higher harmonic component to the base oscillation (3). Hence the information about the phase shift through the 'specimen' is contained in the higher harmonics and the detailed analysis of such components would thus give the phase shift [9]. Especially at a resonance energy, the primary oscillation (3) disappears due to the phase rigidity and higher harmonics are emphasized.

A simpler system is a T-shaped interferometer or a side-coupled geometry drawn in figure 2(b). In an ideal case of this geometry the dot has a single point connection to the interferometer and only the reflection from the dot comes into the interferometer. This means that an in/out process of the dot contains double passing of the dot wavefunction, hence the $0 \to \pi$ shift is doubled to $0 \to 2\pi$ and the resultant phase shift does not reflect the parity of the resonant state in the dot.

A single quantum dot system shown in figure 2(c) does not have an explicit geometrical interference path, though clear interference is observed through a multi-level conduction when the coupling to the wires is strong enough to cause co-tunnelling via an off-resonance state.

2.2. Experimental realization

At present, a high-mobility two-dimensional electron gas (2DEG) at the AlGaAs/GaAs hetero-interface is the best system for realizing solid state electron interferometers. The coherence

length in them is very long and the interference circuits as well as the quantum dots are easily defined by the split gate technique.

A difficulty in the split gate technique arises when a 'floating' gate is an inevitable constituent of the interferometer. The simplest example is an AB ring, where the centre island is inevitably floating. The electrostatic potential of the floating gate fluctuates and is sensitive to those of other gates, muddling the experimental results. A direct way of overcoming the difficulty is the use of a bridging technique, in which a metallic lead passes beyond the sample surface anchoring the electrostatic potential to the voltage source outside the cryostat.

The etching-off method for definition of quantum wires and interference circuits is another way to escape from the difficulty. To define the dots, and to control the parameters, micro-fabricated Schottky gates can be used, which may be split gates or wrapping gates [10]. A problem in the split gate technique is electrostatic coupling between the gates, which disturbs independent control of each gate. Such coupling is usually much smaller in the wrapping gate technique and can be treated as a small linear perturbation. A similar method is selective killing of the 2DEG by oxidation with an atomic force microscope (AFM) [11]. Because of the high resolution smaller dots and circuits are available with this method.

The dot size is controllable by the gate voltages, though a dot from a 2DEG usually has the problem of isolation from the electrodes when it approaches the few-electron regime. Ways to overcome this problem have been reported, e.g. the adoption of very narrow gates though the cleanest dots with high spatial symmetry has been reported for vertical type dots, in which the barrier thickness is determined as that of stacked thin barrier layers and independent of the gate voltage. On the other hand, one meets difficulties in forming the interference circuits with vertical type dots. At present few interference experiments have been reported for vertical type dots.

3. AB ring interferometry

3.1. The Breit–Wigner phase shift

The complex transmission coefficient g at the incident electron energy ϵ around a resonance is expressed in a Breit–Wigner form [12], that is,

$$g(\epsilon) \propto \frac{1}{(\epsilon - \epsilon_0) + \mathrm{i}\gamma}, \tag{5}$$

where ϵ_0 is the resonance energy and γ is a quantity related to the width of the resonance. Equation (5) leads to a steep variation of the phase shift from 0 to π. The first target of the experiments is then to directly detect the behaviour of (5) in the interference.

As mentioned in section 2.1, this phase shift variation cannot be detected as the shift of the AB oscillation phase of a two-terminal AB ring [14], which was clearly demonstrated in pioneering works by Yacoby *et al* [15, 16]. Schuster *et al* first succeeded in demonstrating the phase shift variation that obeys (5) by adopting the open type geometry illustrated in figure 3(a).

At the same time the Weizmann group [13, 15, 16] discovered the intriguing behaviour of 'parity locking' or the 'phase lapse' problem. Figure 3(b) shows the results of phase shift measurement for five successive Coulomb peaks. Around the resonances that are indicated by arrows, the phase shift varies according to (5). It is surprising that the phase shift jumps by $-\pi$ between the resonances and it repeats a $0 \rightarrow \pi$ variation at every peak. Due to the Kramers degeneracy, a single jump of $-\pi$ (or a continuous variation of $-\pi$) is natural, though successive jumps mean that the corresponding wavefunctions stacked in energy have the same parity, which is hardly conceivable within elementary quantum mechanics.

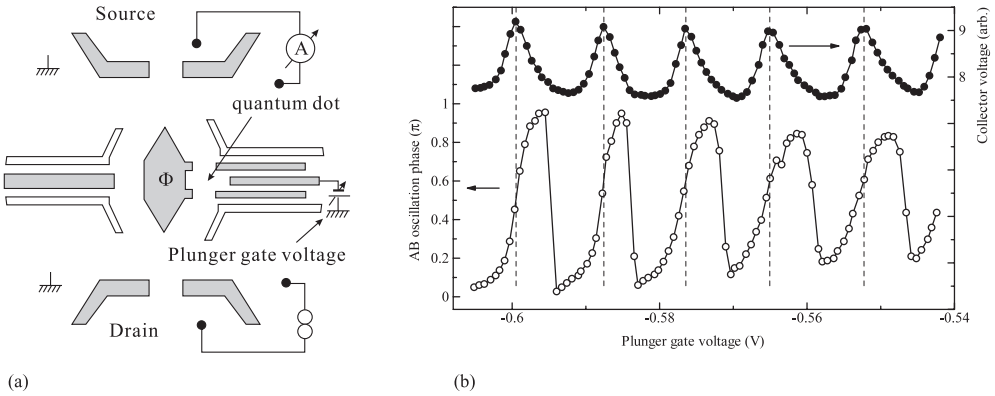

Figure 3. (a) Gate structure of the first device of a multi-terminal (leaky) configuration, in which the phase shift of a QD was measured. (b) Collector voltage which has direct correspondence with the conductance (upper solid circles) and AB oscillation phase (lower open circles) as a function of the dot gate voltage. Data taken from [13].

This phase lapse problem is a challenge both to the theories and the experiments. A number of theoretical proposals have appeared, though most of have not been unchecked by experiments. We will return to this problem in section 6.

3.2. Resonance and transition in two-terminal devices: the Fano effect

In two-terminal devices, the conservation of probability requires that the sum of the total reflection coefficient R and the transmission coefficient T is unity, i.e.

$$T + R = 1, \tag{6}$$

which leads to the phase rigidity mentioned in section 2.1. When the coupling of an AB ring to the leads is weak, the phase rigidity is understood as a result of multiple reflection and circulation of electronic waves inside the ring and the system can be treated as a ring-shaped resonator with a QD and with some leakage to the leads.

This problem falls within so-called 'Fano physics' [17]. Fano [18] treated a scattering problem in which an incident wave is coherently scattered through a localized state with finite coupling to the continuum. In order to extract the effect of resonance between a localized state ϕ and those of the continuum $\varphi(E)$ with energy E, he first wrote down the hybridized state $\psi(\epsilon)$ of the new energy ϵ with coefficients $a(\epsilon)$ and $b(\epsilon, E)$ as

$$\psi(\epsilon) = a(\epsilon)\phi + \int \mathrm{d}E\, b(\epsilon, E)\varphi(E). \tag{7}$$

Here the Hamiltonian H of the hybrid system is defined as

$$\langle\phi|H|\phi\rangle = E_0, \qquad \langle\varphi(E)|H|\varphi(E)\rangle = E, \qquad \langle\varphi(E)|H|\phi\rangle = V_E. \tag{8}$$

Then $b(E)$ is formally written as

$$b(\epsilon, E) = \left[\mathrm{P}\frac{1}{\epsilon - E} + z(\epsilon)\delta(\epsilon - E)\right]V_E a(\epsilon). \tag{9}$$

Though in the usual scattering problem $z(\epsilon)$ is $\mathrm{i}\pi$, here $z(\epsilon)$ can be real as long as the system has time reversal symmetry and is represented as

$$z(\epsilon) = \frac{1}{|V_\epsilon|^2}\left[\epsilon - E_0 - \mathrm{P}\int \mathrm{d}E\, \frac{|V_E|^2}{\epsilon - E}\right] = -\frac{\pi}{\tan\Delta\theta}, \tag{10}$$

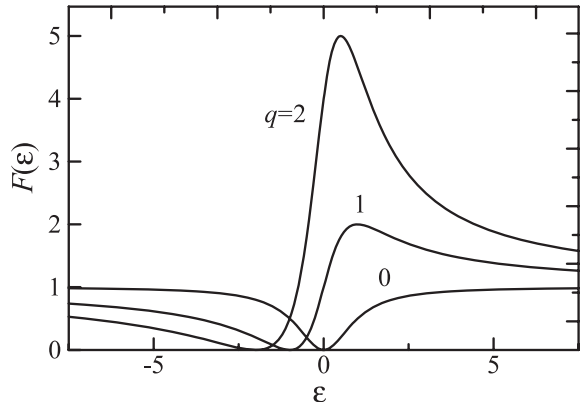

Figure 4. Three typical lineshapes of $F(\epsilon)$ in equation (13) for $q = 0, 1, 2$.

where $\Delta\theta$ is the phase shift due to the coupling V_E. Now the transition probability of an incoming state ξ_i to ψ_ϵ can be written as

$$\langle\psi_\epsilon|T|\xi_i\rangle = \frac{1}{\pi V_\epsilon^*}\langle\Phi|T|\xi_i\rangle \sin\Delta\theta - \langle\psi_\epsilon|T|\xi_i\rangle\cos\Delta\theta, \tag{11}$$

where

$$\Phi = \phi + \mathrm{P}\int \mathrm{d}E \frac{V_\epsilon\varphi(E)}{\epsilon - E} \tag{12}$$

can be interpreted as the localized state modified by the coupling to the continuum.

We obtain the functional form of the transition probability $|\langle\psi_\epsilon|T|\xi_i\rangle|^2$, then, as

$$F(\epsilon') \propto \frac{(\epsilon' - q)^2}{\epsilon'^2 + 1}. \tag{13}$$

Here the energy ϵ' is shifted and renormalized as

$$\epsilon' = -\cot\Delta\theta = \frac{2}{\Gamma}\left[\epsilon - E_0 - \mathrm{P}\int \mathrm{d}E \frac{|V_E|^2}{\epsilon' - E}\right], \tag{14}$$

Γ is the 'width' of the localized state Φ:

$$\Gamma = \pi|V_{\epsilon'}|^2, \tag{15}$$

and the parameter q, which is called the Fano parameter, is defined as

$$q = \frac{\langle\Phi|T|\varphi_i\rangle}{\pi V_{\epsilon'}\langle\psi_{\epsilon'}|T|\varphi_i\rangle}. \tag{16}$$

Typical lineshapes of $F(\epsilon)$ are plotted in figure 4. The phase shift $\Delta\theta$ varies by π around the resonant point E_0 of the localized state, which makes the total system go through a resonance and an anti-resonance (or vice versa). As a result the lineshape has a peak and a dip to zero side by side and is generally largely distorted. $q = 0$ is a special case and $F(\epsilon)$ has only a symmetric dip while it has only a peak when $q = \pm\infty$.

An intuitive view of the relation between the Fano problem and an AB interferometer with a QD is given by considering the case that the QD has a stronger coupling to, e.g., the right electrodes [17]. The localized states in the dot form hybrid states with the continuum in the right electrode and the problem is the transition from the left electrode to the hybrid ones. Here the correspondence with the Fano problem is obvious. Fano's original discussion treated the case

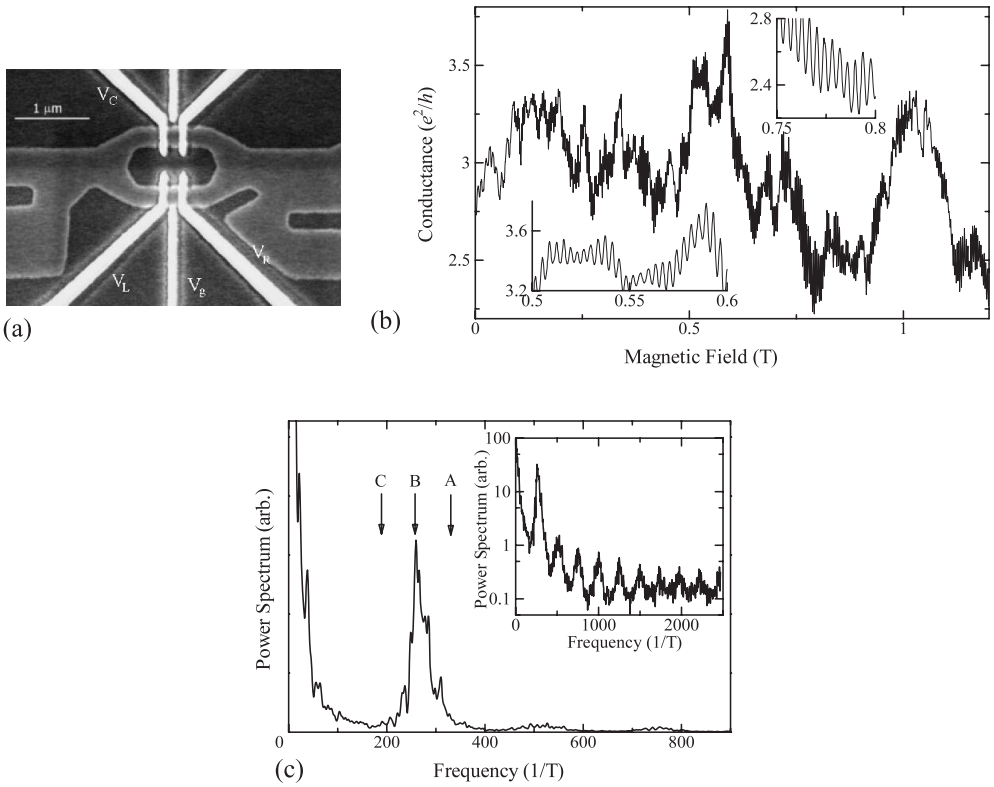

Figure 5. (a) Scanning electron micrograph of the sample used in the observation of the Fano effect in an AB interferometer (ABI). Gate voltages V_L and V_R were used to define a QD in the lower arm whereas V_g and V_C were to control the dot electrostatic potential and the conductance of the reference respectively. (b) Conductance of the ABI, with all the gates at zero voltage. The insets show details for two different regions of magnetic field. (c) Fourier transformation of the magnetoresistance in (b). A, C are the frequencies, which correspond to the outer and inner perimeters of the ABI and B the path goes through the middle of them. The inset is a log-plot of the same data, enhancing the higher harmonics. (From [19].)

with time-reversal symmetry, which corresponds to zero magnetic field. The AB QD problem requires an extension in this point. With such an extension, Hofstetter *et al* [22] obtained a generalized the Fano formula Apart from this specific case, correspondence generally exists between an AB QD system and the extended Fano problem.

Figure 5(a) shows a scanning electron micrograph of our sample made of a 2DEG at an AlGaAs/GaAs interface [20]. The AB ring structure was defined by wet etching and the dot was defined by Schottky gates, which can be seen as white regions in the picture. The dot in the upper arm (the reference path) was not used in the experiment and one of the three gates was used to control the conductance of the reference path.

When we opened all the gates the system worked as an ordinary AB ring interferometer. At the lowest temperature, a clear AB oscillation appeared in the magnetoresistance as displayed in figure 5(b), the Fourier transformation of which shows clear peaks at higher harmonics at least up to 10 (figure 5(c)). This clearly tells us that the paths with large winding numbers contribute to the conductance. The magnetoresistance is highly symmetric to the zero field, reflecting the two-terminal nature of the device (i.e. the Onsager reciprocity). Note that the amplitude of the

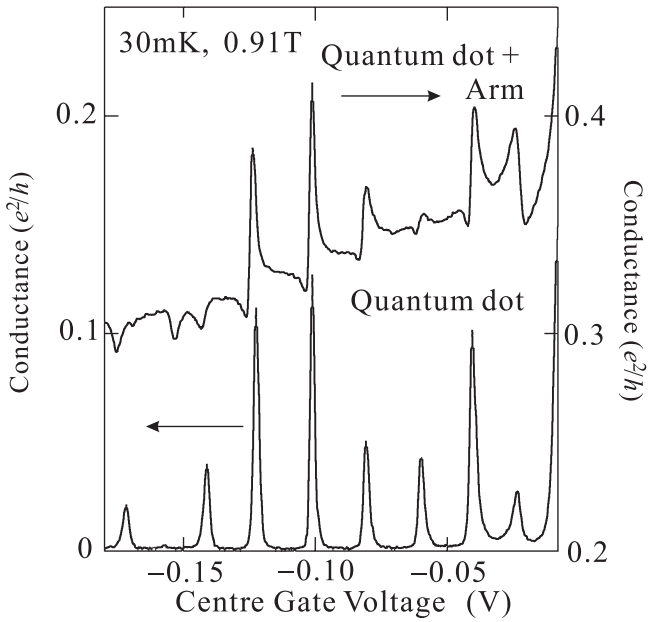

Figure 6. Coulomb oscillations with (upper) and without (lower) parallel conduction of the reference arm. Clear Fano distortion is observed in the data with reference conduction. (From [20].)

AB oscillation remains as 5% of the total conductance due to, e.g., the asymmetry between the two paths (some channels might have no bifurcation at the connections). It should also be noted that the main peak in the Fourier transform has a finite width corresponding to the width of the AB ring geometry. This makes it necessary to consider the multi-path effect, which will be treated in the next subsection.

When the reference arm was pinched off, an ordinary Coulomb oscillation appeared as shown in the lower graph in figure 6, while the lineshape of each Coulomb peak was largely distorted for a finite reference conductance as shown in the upper graph. Equation (13) only tells us the transition probability to the localized hybrid state and the total conductance contains contributions from the other transitions (e.g. a channel with no separation at the wire–ring connection points). Hence the conductance does not 'touch to zero' even at the dips. The evidence that the observed distortion is due to the Fano effect is obtained through the response to the magnetic flux, which can be found in figure 7.

The grey-scale plot in figure 7(a) strongly resembles the theoretical prediction for the Fano effect in an ABI, e.g. in [17], and the pattern is also slightly distorted upward. The distortion means the breaking of phase rigidity, which will be discussed later. A sound demonstration is shown in figure 7(b), where the direction of the distortion is reversed with a magnetic flux variation of $\phi_0/2$. This shows that the distortion comes from the interference through the AB ring and the fact that the Fourier transform of the AB oscillation shows up to 10th higher harmonics leads to the conclusion that the distortion is due to the Fano effect. The lineshapes are well fitted by equation (13), as shown by the broken lines.

An unnatural thing here is that the fitted value of q diverges for the completely symmetric lineshape while the quantities in the right-hand side of equation (16) are hardly believed to go to infinity or zero with magnetic flux. Fano treated the case with time-reversal symmetry, while in the experiment the symmetry is broken by the magnetic flux, hence the extension at this point would solve the unnatural divergence. Such generalization of Fano's theory has been discussed

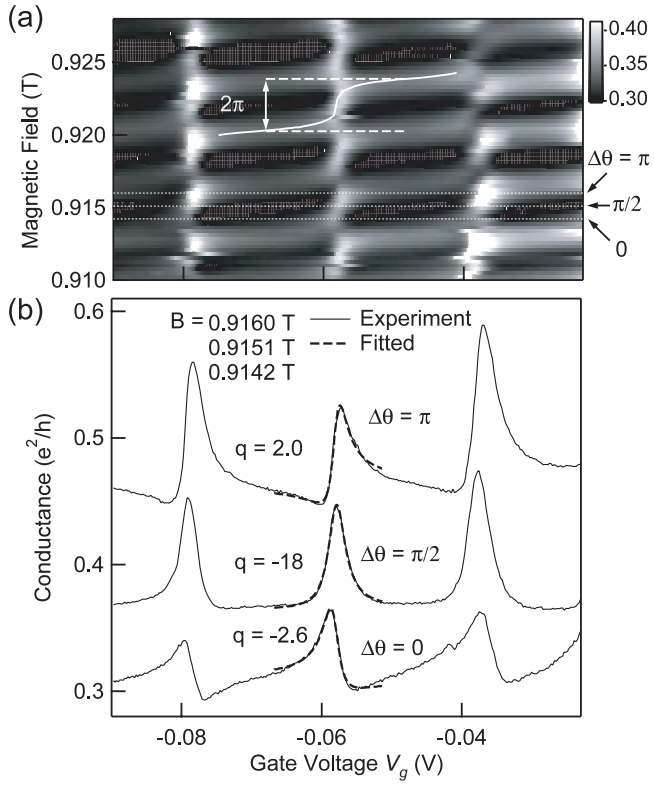

Figure 7. (a) Grey-scale plot of the conductance of the ABI in figure 5(a) as a function of the gate voltage V_g and the magnetic flux. (b) Cross sections of (a) along three white dotted lines, which correspond to the AB phase shift of 0, $\pi/2$ and π. (From [21].)

for years [17, 22–25] and it is suggested that the effect of symmetry breaking can be taken into account by simply modifying the expression of q as

$$q = q_1 \cos(\Delta\theta) + \mathrm{i}q_2 \sin(\Delta\theta), \tag{17}$$

where $\Delta\theta$ is the AB phase shift, q_1 and q_2 are real parameters defined by both the tunnelling coupling between the QD and its leads and the coupling strength between the QD and the continuum energy state. Here q should be treated as a complex number reflecting the broken time-reversal symmetry. We tried fitting the complex qs of equation (17) with equation (13) to the lineshapes around $B = 0.91$–0.93 T. We treated $\mathrm{Re}\,q$, $\mathrm{Im}\,q$, V_0, Γ and the background conductance as fitting parameters [21]. The result of fitting is reasonable, as presented in figure 8(a), as long as we admit q to have an offset, that is, the results shown in figure 8(c) distribute on an ellipsoid with a centre shifted from the origin. This discrepancy with equation (17) is probably due to the multi-path effect discussed in the next section.

3.3. Electrostatic phase shift

As discussed in section 2.1, the biggest obstacle to interferometry using electrostatic phase shift tuning is the energy dependence of the phase shift in equation (2). Hence if there are several channels in an AB ring, the phase shifts are incoherent, which largely disturbs clear interferometry. However, in an AB QD, if each single electron level in the QD has a single

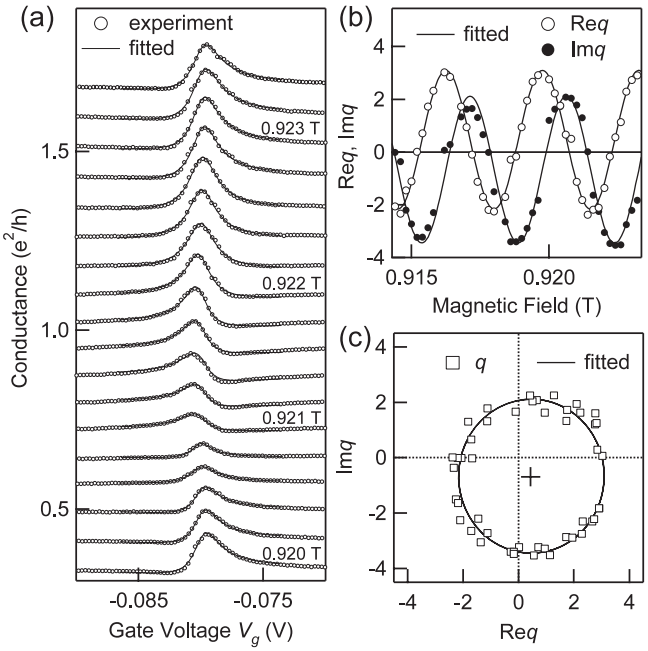

Figure 8. (a) Conductance of the system measured at 30 mK at different magnetic fields that cover one AB period. The open circles and the solid curves are the experiments and the results of the fitting, respectively. They are incrementally shifted upward for clarity. (b) Obtained Re q and Im q are plotted. The solid curves are the fitted sinusoidal curves. (c) Result of (b) plotted in the complex q plane by treating B as an internal parameter. The cross indicates the ellipse centre of the complex q. (From [21].)

channel strongly connected to it, the analysis of Fano lineshape works as an effective filter to extract the interference effect of the single channel.

The above hypothesis can be experimentally checked by applying the 'complex-q' analysis [26]. Figure 9 shows an example of such an analysis. In this experiment the variation of the Fano lineshape was traced by sweeping the control gate voltage V_C, which affects both the electron phase shifts and the conductance through the reference arm. Apparent directional reversal of the distortion due to a shift in V_C is observed in figure 9. As shown in figure 9(b), fitting of equation (13) with real q results in divergent behaviour while complex q smoothly oscillates around zero attesting to successful fitting.

The above results confirm the hypothesis that each level in a QD has a specific channel that has a larger transition probability to it, and at the same time demonstrate that the Fano effect is a powerful tool for filtering conduction channels and extracting the interference of the single channel.

4. Breakdown of phase rigidity in multichannel conduction

The distortion observed in the Fano pattern in figure 7 means a smooth shift of the AB phase, that is, the breakdown of phase rigidity. As mentioned in section 2.1, the constraints that cause phase rigidity in two-terminal devices are equations (3) and (4). Among them the Onsager reciprocity (4) holds well in the experiments, which reflects the two-terminal nature. This simply indicates that (3) is broken and that some multi-path effect breaks the phase rigidity.

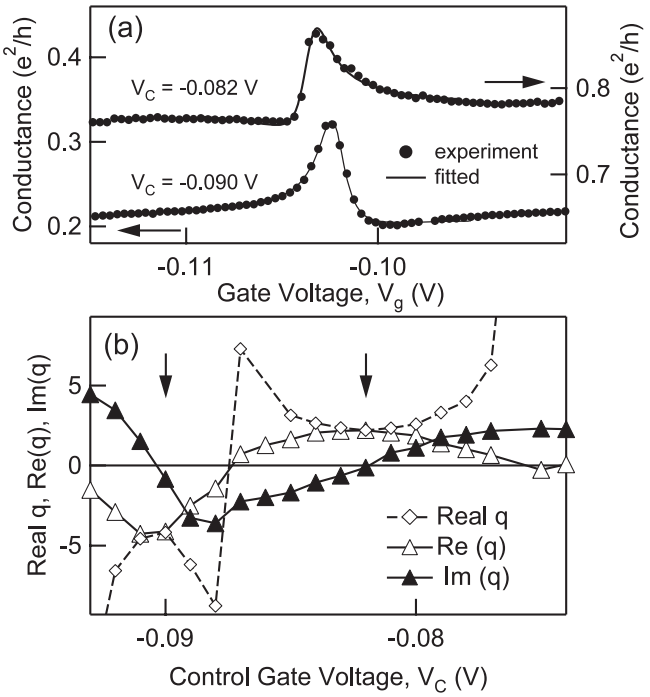

Figure 9. (a) Conductance of an ABI as a function of the dot gate voltage for two different control gate voltages V_C showing a change in the Fano lineshape with V_C. (b) Complex q (i.e. real and imaginary parts) and real q as a function of V_C. While real q shows divergent behaviour, complex q varies smoothly with V_C. The two arrows indicate positions of V_C shown in (a). (From [27].)

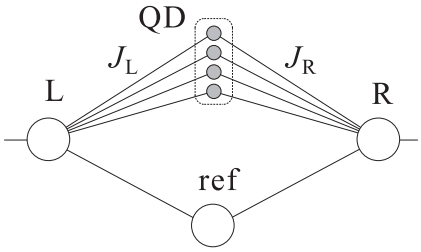

Figure 10. Model for an ABI QD with multichannel conduction: the right and the left leads (R and L) connect to each other via single-electron levels in the QD and, in the reference, independently through $N + 1$ branches (the figure shows the case of $N = 4$).

This is also supported by the width of the Fourier transformation in figure 5(c), which is much wider than the natural width due to the field range.

Aharony *et al* [19] adopted the model shown in figure 10 to consider the multichannel effect, taking into account the hypothesis that each level in the QD has a channel with a strong coupling constant, which was confirmed in the experiment described in section 3.3. In the model, the left and right leads, the reference arm and the levels in the QD are treated as tight-binding sites. The sites in the QD have connections to the left lead (site L) and the right lead (site R) with hopping matrices $J_{\ell,r}(n) = J^0_{\ell,r}(n)\mathrm{e}^{\mathrm{i}\phi(n)}$ with real number $J^0_{\ell,r}(n)$, where ℓ and r correspond to left and right, respectively, n is the index of the levels in the QD,

and $\phi(n)$ is the phase associated with the nth channel. The couplings to the reference are written as $j_{\ell,r}$. Aharony *et al* derived the expression for the complex transmission coefficient t as

$$t = \frac{S_{\ell r} 2\mathrm{i} \sin ka}{(S_{\ell\ell} + \mathrm{e}^{-\mathrm{i}ka})(S_{rr} + \mathrm{e}^{-\mathrm{i}ka}) - |S_{\ell r}|^2}, \tag{18}$$

where

$$S_{xy} = \sum_n \frac{J_x(n) J_y(n)^*}{J[\epsilon - E_D(n)]} + \frac{j_x j_y}{J(\epsilon - E_{\mathrm{ref}})} \tag{19}$$

(x, y stand for ℓ, r), and E_D and E_{ref} are the energies of the dot levels and the reference, respectively. The model in figure 10 seems to be simple, though it can take into account various effects through tuning of the parameters. For example, the effect of a strongly coupling state, which will be discussed in sections 6.1 and 6.2, is effectively included through large $J_{\ell,r}$. Through the interaction via sites L and R, a state with large coupling strength strongly mixes with others and plays the role of a strongly coupled state.

The applicability of the model to experiments was tested by the following procedure [19]. First, the reference arm was pinched off and the parameters except $j_{\ell,r}$ and E_{ref} (e.g. $J_{\ell,r}(n)$, etc) were obtained by fitting equation (18) to the ordinary Coulomb oscillation. Next, the reference was opened and the variation of the Fano lineshape was measured by changing the magnetic field. The fitting of equation (18) to the lineshapes was then attempted with $\phi(n)$, $j_{\ell,r}$ and E_{ref} as fitting parameters. The results are shown in figure 11. The excellent agreement indicates that the model in figure 10 represents the essential points of the physics (e.g. the multichannel effect, and the specific couplings between the paths and the levels).

The present model is applicable for a comparatively narrow range of magnetic field. It assumes rigid conductance channels for magnetic field, which apparently does not hold for a wide range of field. Hence if phase rigidity breakdown occurs uniformly over a wide range of magnetic field, we should consider a different model, as we will see in section 8.3.

5. Interferometry in T-shaped resonators

5.1. The Fano effect in T-shaped geometry

As noted in section 2.1, only the reflection mode wave is contained in a T-shaped geometry interferometer. This makes the situation simple, while the information on, for example, the parity of the wavefunction in resonance is lost. Also, if the connection between a dot and a wire is ideally single, only $q = 0$ is allowed in the lineshape.

On the other hand, the apparent experimental advantage in the T-shaped geometry is that the size of the dot can be extremely small, down to the few-electron regime, while maintaining the coupling strength to an electrode even in lateral QDs without special experimental techniques. This is due to the single-point connection between the wire and the QD, which allows them to be very close to each other. However, this closeness leads to another problem, that is, the effect of electrostatic potential due to the dot. The number of electrons in a QD changes one by one at the Coulomb peaks, which causes a rapid shift of electrostatic potential around the peaks. The shift affects the transport via two channels: the phase shift represented as equation (2) and the changes in the transmission coefficients. As estimated in section 3.3, the former effect is usually smaller than the latter, which is particularly serious when a subband bottom of the wire is close to the Fermi level (i.e. a transition region in the staircase of conductance quantization). Remote charge sensing in QDs usually involves this sensitive region.

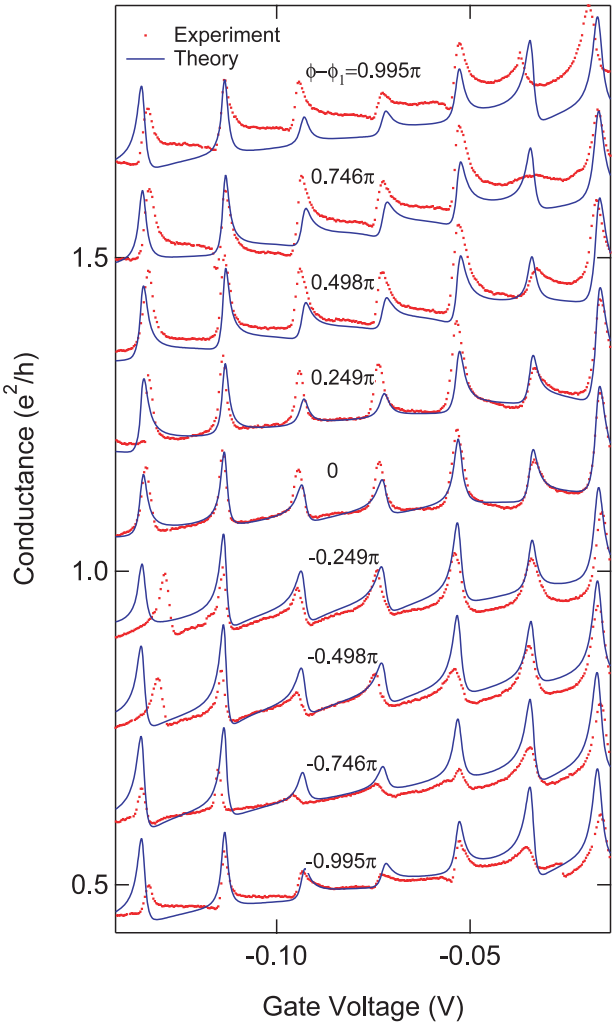

Figure 11. Conductance from the ABI. Dots: experiment. Full lines: fit to theory (equation (18)). Curves correspond to fields B between 0.9100 T ($\phi - \phi_1 = -0.995\pi$) and 0.9132 T ($\phi - \phi_1 = 0.995\pi$), each graph is shifted by $0.15e^2/h$. (From [19].)

Johnson *et al* analysed the conductance of a T-shaped interferometer, accounting for both effects [28]. They found the lineshape to be well fitted by their model, as shown in figure 12, and the Coulomb effect was less serious for stronger coupling between the dot and the wire.

5.2. Temperature dependence of coherence

A T-shape geometry is easily obtained by cutting one end of the QD in an AB ring interferometer by pinching the gate (inset of figure 13(a)). With this method, the 'stub' region tends to become comparatively long, hence the interference pattern appears only at very low temperatures where the coherence length is sufficiently longer than the stub. This behaviour is observed in figure 13(a). Because the crossing point is far from the dot, the Coulomb effect is less effective, which is clearly manifested in the insensitivity to the gate voltage at high temperatures.

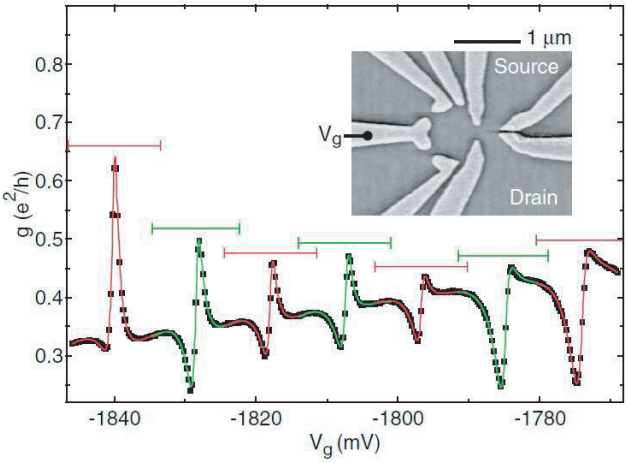

Figure 12. Conductance of a quantum wire with a side-coupled QD (T-shaped interferometer). The inset shows a scanning electron micrograph of the sample. From [28].

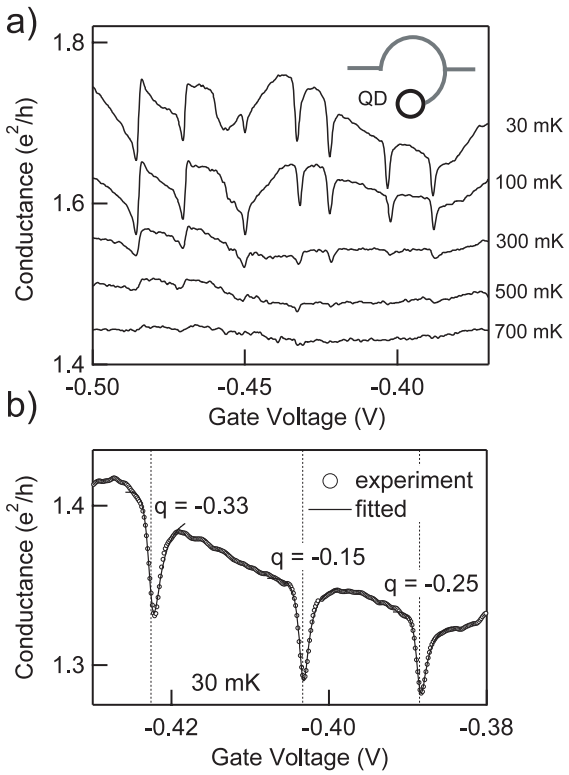

Figure 13. (a) Temperature variation of wire conductance as a function of the dot gate voltage in a T-shaped interferometer with a QD in the end. The inset is a schematic diagram of the sample. A magnetic field of 0.80 T is applied. The curves for $T < 700$ mK are incrementally shifted upward for clarity. When both gates of the dot were open, clear Coulomb oscillation was observed even at 700 mK. (b) Three Fano features in the conductance at 30 mK are fitted to equation (13). The obtained qs are shown. The vertical dashed lines indicate the obtained discrete level positions. From [27].

The simplicity and the long distance for the interference make this system effective for investigating the interference and the temperature dependence of the coherence length. For the gate voltage $V_g > -0.45$ V, almost ideal Fano lineshapes for the side-coupled geometry (single-point contact) with $q \sim 0$ are obtained (figure 13(b)) for many dips, while a significant shift of q from 0 is observed for $V_g < -0.45$ V. We consider the following simple model to take into account the resonance in the stub region in the explanation. Let L be the distance between the T-connection and the dot. The QD is simply expressed as a tunable resonator, which is expressed as a tunnel barrier plus a perfect reflector. The variable phase shift of the reflector is approximated to be proportional to the gate voltage around resonance. The quantum wire between the dot and the T-connection is simply a phase shifter of kL (k is the wavevector). We set the S matrix for the T-connection $\boldsymbol{S}_T$ as

$$\begin{pmatrix} b_1 \\ b_2 \\ b_3 \end{pmatrix} = \boldsymbol{S}_T \begin{pmatrix} a_1 \\ a_2 \\ a_3 \end{pmatrix}, \qquad \boldsymbol{S}_T = \begin{pmatrix} \frac{1-a}{2} & -\frac{1+a}{2} & \sqrt{\frac{1-a^2}{2}} \\ -\frac{1+a}{2} & \frac{1-a}{2} & \sqrt{\frac{1-a^2}{2}} \\ \sqrt{\frac{1-a^2}{2}} & \sqrt{\frac{1-a^2}{2}} & a \end{pmatrix}, \tag{20}$$

to maintain the unitarity. Here, we take a to be a real number, which determines the direct reflection coefficient. The S matrix for the quantum wire (phase shifter) is expressed as

$$\begin{pmatrix} a_3 \\ b_3' \end{pmatrix} = \boldsymbol{S}_{QW} \begin{pmatrix} b_3 \\ a_3' \end{pmatrix}, \qquad \boldsymbol{S}_{QW} = \begin{pmatrix} 0 & e^{i\beta} \\ e^{i\beta} & 0 \end{pmatrix}, \qquad \beta \equiv kL. \tag{21}$$

The S matrix for the tunnel barrier can be written as

$$\begin{pmatrix} a_3' \\ a_4 \end{pmatrix} = \boldsymbol{S}_D \begin{pmatrix} b_3' \\ b_4 \end{pmatrix}, \qquad \boldsymbol{S}_D = \begin{pmatrix} \cos\phi & i\sin\phi \\ i\sin\phi & \cos\phi \end{pmatrix}. \tag{22}$$

Lastly, the reflector with a variable phase shift of θ is simply expressed as

$$b_4 = e^{i\theta} a_4. \tag{23}$$

By calculating the combined S matrix, the complex transmission coefficient of the system is obtained as

$$t = \frac{1+a}{2} \cdot \frac{-1 - e^{i(\theta+2\beta)} + (e^{2i\beta} + e^{i\theta})\cos\phi}{1 + a e^{i(\theta+2\beta)} - (a e^{2i\beta} + e^{i\theta})\cos\phi}. \tag{24}$$

It is easy to see that equation (24) leads to non-zero q if we approximate the lineshape with equation (13). We utilized the expression (24) to calculate the temperature dependence of the lineshape resulting from the thermal broadening of electron energy, and found the temperature variation shown in figure 13(a) to be well explained by the thermal broadening. That is, the temperature dependence of the Fano lineshape is well fitted by

$$G_{Fano} = A\frac{2e^2}{h} \int d\epsilon |t(\epsilon)|^2 \frac{1}{4k_B T} \cosh^{-2}\left(\frac{\epsilon - \mu}{2k_B T}\right), \tag{25}$$

where μ is the Fermi energy (see figure 14). In other words, there is no trace of additional 'intrinsic' decoherence [29] in the present case.

5.3. Interferometry for a few-electron QD

When the dot is very close to the branch, the Coulomb effect is severe; on the other hand, this can be utilized for the charge detection of the charge state in the QD. The Coulomb effect is greater at transition regions between quantized plateaus, and the main effect switches to the interference on the plateaus. However, the step-like conductance variation with the wire gate voltage is still mainly determined by the number of conductance channels, and the interference

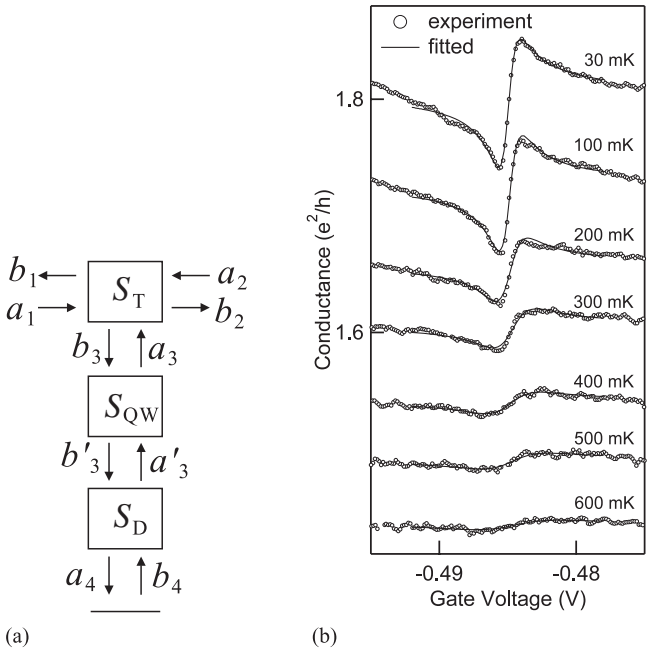

Figure 14. (a) Theoretical model used to analyse the temperature dependence of the Fano lineshape in a T-shaped interferometer. Rectangles represent S matrices. (b) Results of fitting of equations (24) and (25) to the data.

effect and the Coulomb effect appear as small corrections to the conductance. In order to extract the Coulomb and interference effects of the dot on the wire conductance, we extract such simple stepwise conductance from the total conductance. The residual shift is plotted in grey scale in figure 15(a), as a function of the wire gate voltage (V_w) and the dot gate voltage (V_g).

In figure 15(a), black and white stripes run along the V_w axis with some slanting and complicated crossing. They correspond to the Coulomb oscillation of the dot with Fano distortion. Such flows along V_w suddenly disappear for $V_g < -1.0$ V. This region is assigned to the number of electrons in the dot N being zero. Charge sensing measurement supports this assignment. The indices of conductance quantization are noted as M in the figure and the curving of the Fano lines occurs in the transition region of M. The amplitude of the oscillation against V_g is higher in these regions due to the Coulomb effect, i.e. charge sensing. The amplitude of the oscillation falls sharply at the last Fano line, which means no change occurs in N below this gate voltage, namely, $N = 0$.

In the plateau regions, the Coulomb effect is less severe and the subband number in the wire is stable resulting in regular Fano lines. The addition energy spectra can hence be obtained from the distances between the Fano lines. Figure 15 shows the obtained addition energy as a function of N for various V_w. Apparent peaks exist at $N = 2$ and 6, which correspond to the closed shells of the two-dimensional circular harmonic potential. This result indicates that, unexpectedly, circular potential is formed in this side-coupled geometry.

We focus our attention on the Fano structure at the $M = 1$ plateau. Figure 15(c) is a close-up of the data for that region. The crossings of black and white lines mean that a rapid change of the sign of q occurs around the middle of the plateau. In the previous section, we observed that an extra resonator between the wire and the QD causes shifts from $q = 0$. However, this model is not realistic for the present case because the dot and the wire are too close to each

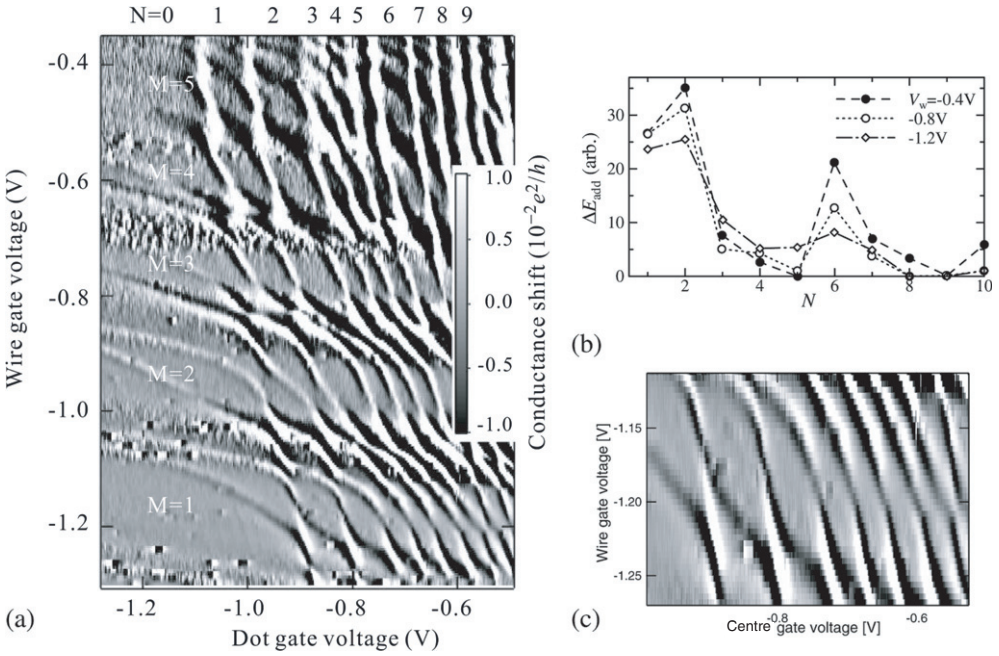

Figure 15. (a) Grey-scale plot of the wire conductance shift from ordinary stepwise-varying conductance of a QPC as a function of the dot gate voltage and the wire voltage. M indicates the index of conductance quantization of the wire and N the number of electrons in the dot. Fano peaks appear as strong black–white stripes. Data taken from [30]. (b) Addition energy spectra of the dot obtained from the distances between the Fano peaks in (a) for three difference wire gate voltages. (c) Close-up of (a) around $M = 1$.

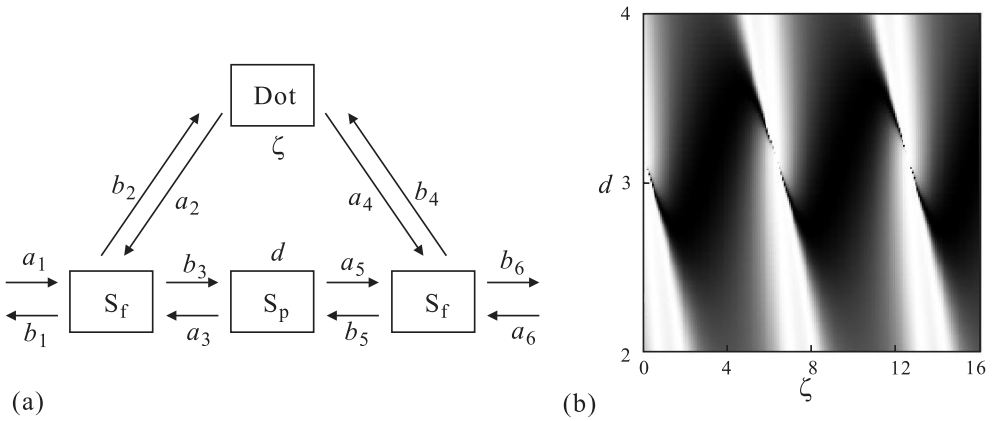

Figure 16. (a) Theoretical model of a side-coupled dot–wire system. A single channel is assumed in the wire and in the multiple connections to the QD. Rectangles indicate S matrices. S_f are fork matrices, which are identical to $\boldsymbol{S}_T$ in equation (20). The dot S matrix is composed of two barrier matrices ($\boldsymbol{S}_D$ in equation (22)) and a phase shifter ($\boldsymbol{S}_{QW}$ in equation (21)) and the phase shift is ζ. S_p is also a phase shifter with a phase shift of d. (b) Grey-scale plot of the calculated transmission of the system in (a) as a function of phase shifts ζ and d. White corresponds to 1 and black to 0. Note the similarity to figure 15(c).

other to have another resonator between them. Here, we instead consider the finite 'width' of the contact. The simplest model is expressed by the diagram shown in figure 16(a). On

a conductance plateau, only the wavenumber along the wire varies with the gate voltage, and this causes a phase shift between two S matrices, which results in the change in the sign of q. Note that this simple model does not hold on higher plateaus where the multichannel effect is predominant, and indeed, in the results (figure 15(a)), no such simple pattern is observed for the plateaus with $M > 1$.

6. Interferometry in nearly open QDs

In this section, we focus on the parity of the wavefunction, which appears in the transmission phase. The key phenomenon is the 'phase lapse' introduced in section 3.1. Here we introduce theoretical interpretations and present experimental evidence for the key concept in some of them.

6.1. Strongly coupled state and 'phase lapse' problem

As noted in section 3.1, an important and intriguing problem revealed by the Weizmann experiments is the 'phase lapse' or 'parity locking' problem. As summarized in [31], the theoretical approaches can be roughly classified into two groups.

In the first group, the existence of a few special states that have much stronger couplings with leads than do other states is assumed. The legitimacy of such an assumption in a certain range of dot parameters, particularly for two-dimensional QDs, was verified by numerical simulations [32–34]. Roughly summarized, the low symmetry or distortion of the confinement potential leads to a spatial distortion in the localized wavefunction, and if a wavefunction happens to have a high amplitude connecting the two leads attached to the dot, the transmission coefficient through the state can be much larger than the others. Here we call such states strongly coupled states (SCSs), and other states weakly coupled states (WCSs).

For the second group, elastic co-tunnelling at the Coulomb valleys is seriously considered [35]. A large number of eigenstates in the dot may contribute to such transport, and they are random in phase and amplitude though the situation changes very little in a series of consecutive valleys leading to the repetitive $-\pi$ jumps of the phase shift in the middle of the Coulomb valleys.

It is easy to show that the parities of transmission through WCSs are dominated by the SCS nearest in energy. This can be inferred in a single-electron picture [34]. Let us take an artificial dot confinement potential V_0 that has a small difference V from the real potential and let $\{\psi_j^0\}$ be the eigenfunctions. We can take V_0 so as not to have high spatial symmetries and then the existence of SCSs in $\{\psi_j^0\}$ can be expected. We treat V as an artificial perturbation. The wavefunction of a WCS after mixing is expressed in the first order as

$$\psi_j \approx \psi_j^0 + \psi_N \frac{\langle \psi_j^0 | V | \psi_N \rangle}{E_j^0 - E_N}, \tag{26}$$

where N is the index of the SCS closest to the energy level E_j^0 of the unperturbed state ψ_j^0. Because the couplings to the electrodes are much stronger for ψ_N, the matrix element for the transition through ψ_j is dominated by the component that contains $|\psi_N\rangle\langle\psi_N|$. The point of this discussion is that from the aspect of transport, SCSs dominate the states even when the absolute value of the component is not very large.

The above concept explains parity locking for several peaks under the domination of an SCS, though there should be parity alternations when the nearest SCS is replaced by the next one. A concept to explain the parity locking for a number of peaks is 'state hovering' over the Fermi level, which is illustrated in figure 17. We consider electron–electron interaction

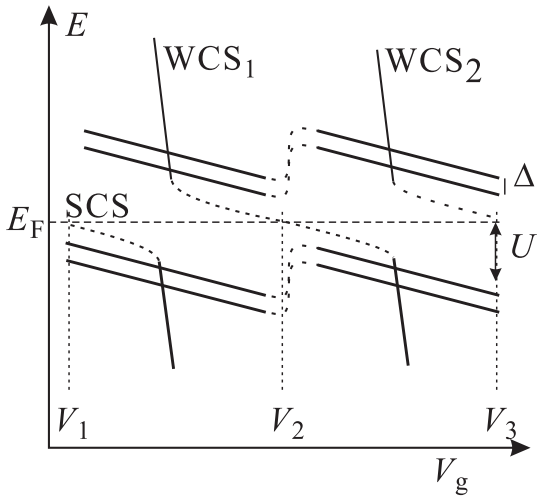

Figure 17. Schematic diagram to explain the concept of 'state hovering' of energy levels in a QD as a function of gate voltage. Redrawn from [36].

in the simplest static capacitance approximation. Because an SCS has strong couplings to the electrodes, its spatial dimensions should also be larger than those of WCSs, resulting in a slower movement along the energy axis against the gate voltage. This causes many crossings between the SCS and WCSs, though the coupling through electrodes causes anti-crossing, which transfer, for example, the SCS component from the lower branch to the upper one. When several conditions are fulfilled, this raises the SCS at the anti-crossing and the level that crosses the Fermi level always has the character of the SCS.

A weak point of this explanation is that the 'hovering' is not stable to the fluctuation of parameters. Several stabilization mechanisms for the hovering or a similar phenomenon have been proposed. Under the condition

$$\Gamma_{\mathrm{WCS}} \ll \Delta \ll \Gamma_{\mathrm{SCS}} \ll U. \tag{27}$$

Silvestrov and Imry pointed out that the energy due to the quantum fluctuation through the SCS (second-order perturbation) and the constant Coulomb energy U leads to rapid population switching in Coulomb valleys and stable hovering [33]. This line of thought has been extended to include, for example, the asymmetry of electrodes [37]. Baltin *et al* also discussed that the finite temperature would also stabilize the hovering [35].

6.2. The Fano effect without an interference circuit

In this subsection, we present an experiment to prove the existence of SCS in a QD.

Göres, Goldhaber-Gordon and co-workers were the first to claim the observation of the Fano effect in a fabricated semiconductor QD, though their device had no outer interference circuit [38, 39]. This opened up many theoretical proposals for the interpretation. Although in many of those proposals the appearance of the Kondo effect is assumed, here we discuss another possibility together with the presentation of our experiment.

When the connection of a QD to leads becomes stronger and approaches e^2/h, which is the boundary to an open dot, the co-tunnelling conductions via SCSs become very large and comparable to those through resonant levels. In such a case, interference between a resonant-level conduction and a co-tunnelling using the SCS nearest in energy would take place, resulting in the Fano effect. Note that in this regime the SCS closest to the Fermi surface is broad in

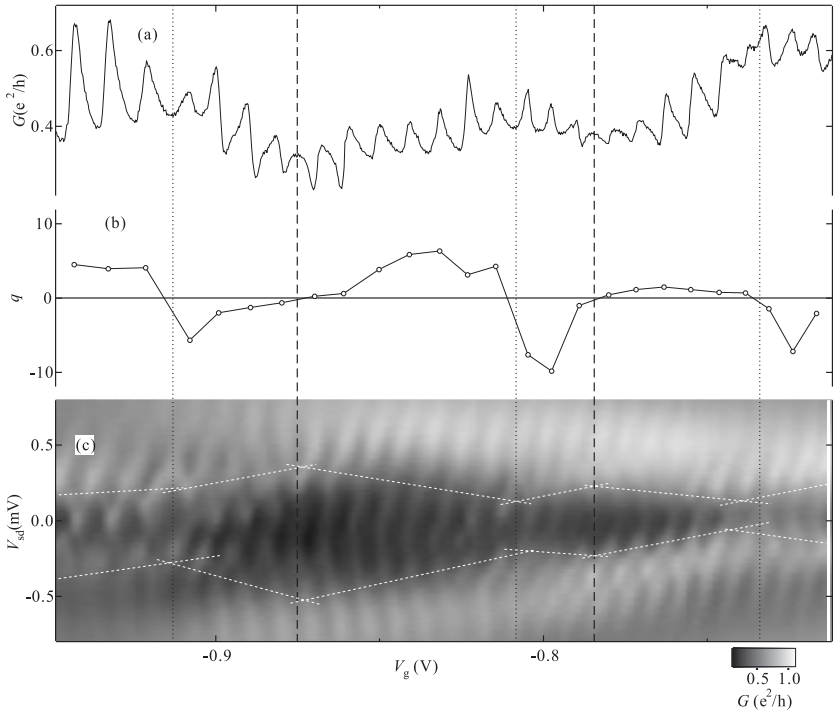

Figure 18. (a) Coulomb oscillation of a quantum dot marginally inside the 'closed dot' region. The slow background oscillation is due to the series of SCSs. (b) Fano parameters q obtained by fitting equation (13) to each lineshape. Vertical dotted and broken lines indicate the zero-crossing points, which are in accordance with peaks and dips of the background oscillation in (a). (c) Grey-scale plot of the conductance as a function of the gate voltage and the source–drain voltage, showing stacked Coulomb diamonds (the stacking is due to the Fano distortion). The edges of Coulomb blocked regions are roughly connected by white broken lines, which reveals larger diamond structures. (After [40].)

energy and in real space, hence condition (27) is not fulfilled and the stabilization mechanism of state hovering is not in effect.

We prepared a simple single-dot structure (figure 2(c)) and the conductance was set to immediately below e^2/h. Figure 18(a) shows the Coulomb oscillation for zero-bias conductance in a wide range of gate voltages V_g. The sawtooth-like patterns are Fano-distorted Coulomb peaks and they are superposed on a slow irregular background oscillation with a large amplitude. From the fitting of equation (13) to each peak, we obtain the values of distortion parameter q and plot them in figure 18(b). The obtained parameter also oscillates coherently versus V_g, but out-of-phase with the background oscillation as indicated by the vertical dotted and broken lines.

Our speculation gives qualitative explanations for all the above observations. Because stabilization of state hovering is 'off', the SCSs move slowly with V_g, resulting in the slow background oscillation. A replacement of the closest SCS then occurs in the valleys of the background oscillation. The sign of q represents the direction of the transition in the interference, i.e. destructive to constructive or vice versa. Although the hovering is off, the anti-crossing between the closest SCS and the resonant WCS should occur somewhere close to the Fermi level, giving the opposite parity to the WCS (i.e. parity domination by WCS with state mixing). Now the phase shift of a dominating SCS varies by π around the corresponding

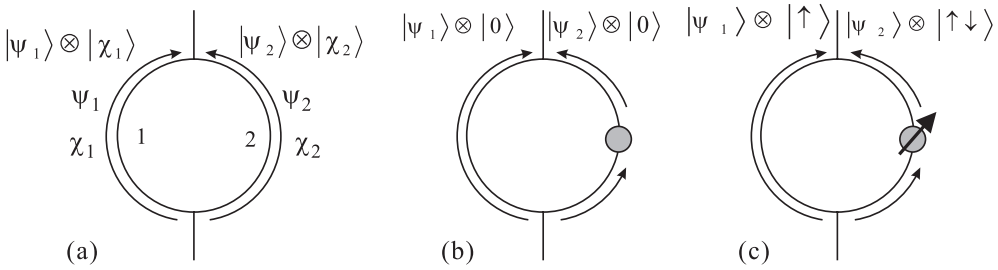

Figure 19. (a) Simple model for describing quantum decoherence in an AB ring. $\psi_{1,2}$ correspond to electron wavefunctions and $\chi_{1,2}$ to the environment. (b) We take a QD in path 2 as an environment. If there is no spin in the QD, the QD quantum state is not charged with the passage of an electron. (c) When the QD has a spin, the traversal of an electron creates the states superposition $(|\uparrow\rangle - |\downarrow\rangle)/\sqrt{2}$ in the QD. As a result, the amplitude of the interference term largely decreases (partial coherence).

peak of the background oscillation. Let us consider the case when an SCS is approaching E_F by the gate voltage and has the phase shift 0. The phase shift of a WCS changes from π to 0 when it crosses E_F, resulting in positive q (destructive to constructive). Then after the SCS passes E_F (a peak in the background), the sign of q should be reversed. In other words, $q > 0$ to the left of a background peak and $q < 0$ to the right. This is exactly what we observe in figures 18(a), (b). Note that the interference occurs between an SCS and a kind of 'mirrored state' and this direction of sign change in q should be generically observed [34].

The above inference is further supported by the Coulomb diamond measurement shown in figure 18(c), in which diamonds originate as a result of Coulomb blockade between adjacent WCSs lined up in a stacked manner due to Fano distortion. The closer the energies of an SCS and a WCS, the greater the mixing. Because an SCS has a larger spatial scale, greater mixing results in smaller effective capacitance, that is, smaller diamond size. This leads to an oscillation in the size of diamonds that is synchronized with the background oscillation. These features are also clearly observed and confirm that the above discussion is on the right track.

We hence conclude that the above results clearly indicate the existence of SCSs in QDs and the domination of parities in the transport.

7. Spin–flip scattering

So far, we have considered phase shift in the orbital part of the electron wavefunction. When there are some factors that affect the spin part, such as spin–flip scattering and spin–orbit interaction, the inner product of the spin part also causes interference depending on the mutual angle of spins. Hence a perturbation that modifies the spin angle can serve as a variable for tuning the interference.

The simplest way to tune the interference of such a spin part is to apply a local magnetic field to a path in an interferometer. A local field causes rotation of spins on one of the interference paths and affects the output. Such experiments were carried out using neutron beams in the 1970s [41, 42].

A QD with an odd number of electrons has a localized spin of 1/2 at least. If the dot is embedded in one of the interference paths and the localized spin interacts with those of conduction electrons, the spin part is also affected, and that is evident in the output.

We can consider the process to be quantum decoherence, as follows. In a sense, decoherence of a quantum system ψ occurs through entanglement with the 'environment' χ,

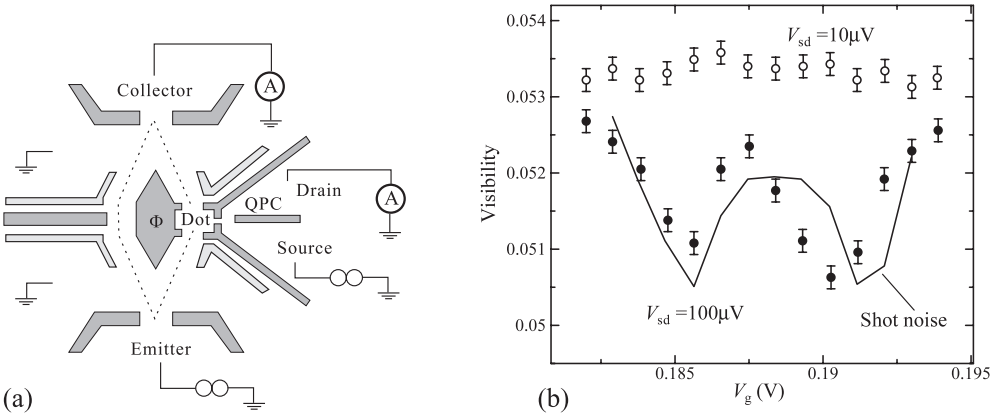

Figure 20. (a) Schematic of gate configuration (grey regions) adopted in the Weizmann group experiment to detect decoherence due to observation via a QPC adjacent to a QD. (b) Visibility of AB interference as a function of QPC gate voltage for two source–drain voltages (10 μV: open circles, 100 μV: solid circles). The solid line shows the shot noise level in arbitrary units. The data are taken from [44].

which has an infinite number of degrees of freedom [43]. Let us take, for example, an open AB interferometer and assign ψ_1 and ψ_2 for electron traversals through paths 1 and 2, respectively (figure 19). If we ignore the environment, an electron traversing over the ring is then expressed as the sum $|\psi_1\rangle + |\psi_2\rangle$. The environment wavefunctions $\chi_{1,2}$ are introduced in the same manner and the total wavefunction Ψ is written as the sum of direct products:

$$|\Psi\rangle = |\psi_1\rangle \otimes |\chi_1\rangle + |\psi_2\rangle \otimes |\chi_2\rangle, \tag{28}$$

$$\langle\Psi|\Psi\rangle = |\psi_1|^2 + |\psi_2|^2 + 2\,\mathrm{Re}[\langle\psi_1|\psi_2\rangle\langle\chi_1|\chi_2\rangle]. \tag{29}$$

The last term represents the interference. Equation (28) is a quantum entangled state if χ_1 and χ_2 are not identical. If χ_1 and χ_2 are orthogonal, equation (28) represents a maximally entangled state and the interference term in equation (29) vanishes. This process can be decoherence because the environment has a infinite number of degrees of freedom and the interference does not recover henceforth.

The observation of such a decoherence was demonstrated by the Weizmann group using a QD in an open AB interferometer. They placed a quantum point contact (QPC) next to the QD to detect the charge states in the QD by conductance through the QPC (figure 20(a)). They found a clear correlation between the shot noise in the QPC conductance and the AB visibility, as shown in figure 20(b). In this experiment, the numerous electrons flowing through the circuit that contains the QPC play the role of the environment.

The quantum decoherence observed in the low-temperature limit in quantum transport has often been attributed to spin scattering at local magnetic moments, though the debate on 'intrinsic decoherence' has not been completely settled [45]. In spin–flip scattering, a local moment 'memorizes' the spatial path of an electron and this information spreads out by the following interaction with other degrees of freedom. It was theoretically proposed that such a spin–flip decoherence mechanism can be microscopically verified using a QD embedded in an AB ring [46–49]. Here, a QD with an odd number of electrons serves as a magnetic impurity. A traversing electron becomes decoherent only when it undergoes spin–flip scattering and 'partial coherence' should remain, though this mechanism certainly diminishes the AB amplitude. Therefore, the AB visibility should be lower for states with an odd number of electrons.

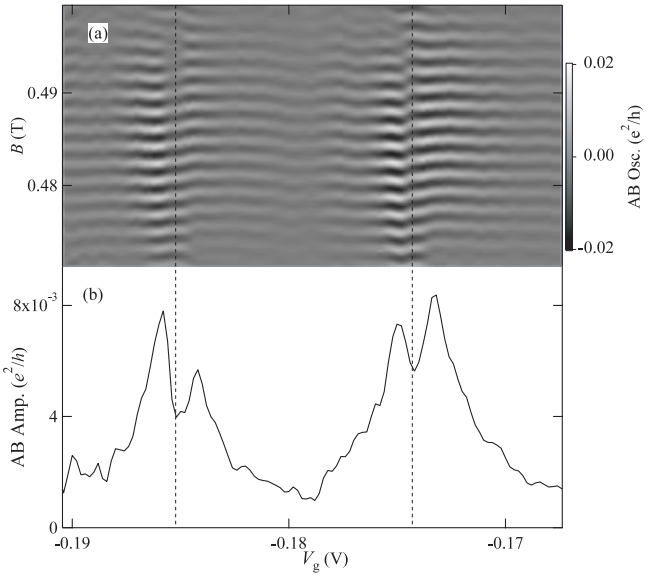

Figure 21. (a) Grey-scale plot of the AB component of conductance in a ring-and-dot system. Two vertical dotted lines indicate the positions of twin Coulomb peaks (a spin pair). (b) Integrated AB amplitude around spin-pair states. The dip structures exactly at the peaks are due to the phase jumps originating from the phase rigidity. (From [54]).

In spite of the simple principle of detecting partial coherence, the experimental realization has many obstacles. The above scenario is highly idealized in that all aspects of the system and environment other than the occupation of the topmost level are assumed to be identical throughout the entire region of Coulomb peaks. In the actual experiment, it is crucial to assess to what degree this condition is fulfilled. There are many factors that might affect the AB amplitude as a function of N, such as a change in the electrostatic potential. The assumed energy level structure, that is, a non-degenerate nearly equidistant stack based on the random matrix theory [50], rarely holds for semiconductor QDs [51], and electron correlation can give rise to high-spin states. Therefore, the simple picture that single-electron orbital levels are sequentially occupied by spin-up and spin-down electrons is far from reality.

Nevertheless, one can hope to find an energy window (i.e. the gate voltage) within which the simplest 'spin-pair' model is a good approximation: only a single Kramers degenerate state should exist immediately above a closed-shell many-electron state in the energy diagram. Although such a spin-pair state rarely exists in semiconductor QDs [51–53], once it is found we can circumvent the above problems and attribute the difference in the coherence to spin entanglement, because the conditions other than the spin state are ideally equal for both sides of Coulomb peaks in this window.

A spin-pair state appears as twin Coulomb peaks (spin-pair peaks). The conditions required of such twin peaks are as follows. (I) They should be entirely alike with each other in the magnetic field dependence of the positions and the heights. (II) The above dependence should be different from those of neighbouring ones because the conductions at neighbouring peaks are through different single-electron orbital states. (III) The addition energy between the peaks is likely to be smaller than those of neighbouring peaks because there should be no portion of orbital energy. Note that condition (II) excludes high-spin states.

Following the above guidelines, we searched for such a spin-pair state in a QD embedded in a two-terminal AB ring and found one from among hundreds of Coulomb peaks [54]. Figure 21

shows the result of AB measurement around the spin-pair states. The dips exactly at the Coulomb peaks are due to AB phase jumps originating from the phase rigidity. Asymmetry in the amplitude is clearly observed, which indicates the reduction of coherence through the conductance over the state with an odd number of electrons. This observation is evidence of the decoherence mechanism involving spin–flip scattering.

The spin–flip decoherence mechanism is effective in the absence of the Kondo effect, which prevents the quantum information of scattered electrons from spreading out to the environment. We continue this discussion in the next section.

8. The Fano–Kondo effect in quantum dot systems

8.1. The Kondo effect in a quantum dot

Immediately after a scattering of a conduction electron $|s, \downarrow\rangle$ by a localized spin $|d, \uparrow\rangle$, an entangled state,

$$\frac{1}{\sqrt{2}}(|s, \uparrow\rangle|d, \downarrow\rangle - |s, \downarrow\rangle|d, \uparrow\rangle), \tag{30}$$

is formed. At this moment, the state is still expressed by a vector in Hilbert space and the scattering itself cannot be counted as quantum decoherence. The decoherence thus requires some additional mechanism to disperse the quantum information memorized on the dot into the environment. Therefore if one adopts a theoretical formalism, that has no such built-in mechanism for decoherence, as a tautologous conclusion, no decoherence appears. In such theories, spin scattering is nothing but spin rotation and a reduction in the interference amplitude is merely due to another interference effect in the spin part, and apparently they are not applicable to realistic systems with spin scattering.

However, when the Kondo effect takes place, the situation changes. As is well known, the spin-scattering process, equation (30), is one of the origins of the Kondo effect [55, 56]. Upon lowering the temperature below the characteristic T_{K}, a many-body state that screens the local moment grows. The state called the Kondo cloud (ψ_{Kondo}) can include the Fermi liquid state (ψ_{Fermi}), for example, by the following procedure [57]:

$$\psi_{\mathrm{Kondo}} = \left\{\sum_k [\Gamma_k^{\alpha} a_{k\downarrow}^{\dagger}\alpha + \Gamma_k^{\beta} a_{k\uparrow}^{\dagger}\beta] + (\text{higher order terms})\right\}\psi_{\mathrm{Fermi}}, \tag{31}$$

where α and β denote spin-up and spin-down states, respectively. The first term on the right-hand side represents the first-order spin scattering, equation (30), and the sum of all order terms represents a *closed* many-body state with a huge number of entanglements. In this sense, the Kondo effect is a disturbance mechanism of the dispersion of the quantum information memorized on the dot into the environment. This 'recovery' of coherence is not equivalent to the screening of the local moment, in that the coherence also recovers even in the case of over/underscreening.

In a spin-1/2 Kondo model in particular, a Kondo cloud is in resonance with the Fermi surface of conduction electrons. Therefore, the conductance through a Kondo cloud is locked to the quantum conductance $2e^2/h$ in the unitary limit, resulting in the characteristic Coulomb oscillation shown in figure 1(c). At the same time, reflecting the resonant feature, the phase shift attaches to $\pi/2$, which is derived using the Anderson theorem and the Friedel sum rule. This behaviour is a direct reflection of 'resonance' and thus reflects the many-body nature of the Kondo effect.

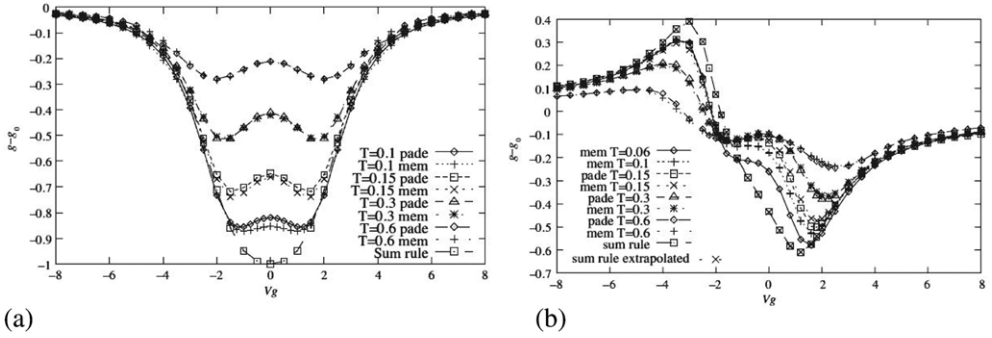

Figure 22. Fano–Kondo lineshape calculated for a T-shaped geometry with a tight-binding approximation. (a) Parameters (energy ϵ, on-site repulsion U, hopping matrix elements t_{ij}) of the T-connection site are the same as those of neighbouring sites. The Fano parameter q should consequently be zero. Temperature dependences are calculated by various approximation methods (Padé, maximum entropy method (MEM)). The curve for absolute zero is deduced from the Friedel sum rule. (b) With shifting of the parameters from the symmetric point, a FK lineshape with non-zero q appears. In the present case, $U_d = 4$, $\delta/t = 1$, $\delta_d/t = 0.61$, and q becomes -0.8. The plateau structure due to $\pi/2$ phase shift locking is observed at low temperatures. (From [58].)

8.2. The Fano–Kondo effect in a T-shaped geometry

An anomalous behaviour of the phase shift should appear in the interference effect. When a quantum dot is part of a quantum mechanical resonant circuit and the spin in the dot brings about the Kondo effect, the geometrical (i.e. single-electron) resonance and the many-electron resonance should coexist, resulting in a peculiar lineshape of the transmission, called the Fano–Kondo (FK) effect [22].

If we assume the simplest dot level structure, that is, a stack of spin-pair states, the Kondo effect appears alternately in Coulomb valleys, reflecting the fact that the local spin $1/2$ only appears for a dot with an odd number of electrons. This results in alternating enhancement of conductance in the Coulomb valleys as shown in figure 1(c). If we put such a Kondo dot in an interferometer, the FK lineshape should appear alternately (figure 1(d)).

In an ideal T-shaped interferometer that has a single-point contact between the lead and the dot, only the $q = 0$ Fano effect is allowed. In this case, the FK lineshape should be the upside-down form of the symmetric Kondo lineshape. However, as discussed in sections 5.1 and 5.3, we often observe a $q \neq 0$ Fano effect in the T-shaped geometry. This occurs, for example, as a result of the presence of an extra resonator between the T-coupling position and the dot. In a tight-binding approximation, this corresponds to setting parameters different from those of the neighbouring ones at the site exactly at the T-coupling position [58]. Figure 22 shows the results of such a calculation. Each site has its own orbital kinetic energy ϵ, on-site Coulomb repulsion U, and hopping probabilities to neighbours t_i. When these parameters are set to be uniform along the quantum wire, q is zero and the FK lineshape is simply the upside-down form of the ordinary Kondo lineshape, whereas when q is non-zero, a peculiar FK lineshape with a plateau due to $\pi/2$ phase shift locking appears, as shown in figure 22(b).

We measured the conductance of a quantum wire placed adjacent to a quantum dot (figure 23(a)) [59]. The coupling between the dot and the wire can be tuned via the gate voltage V_m. Figure 23(b) displays the wire conductance for different coupling gate voltages V_m as a function of the dot gate voltage V_g. The wire gate voltage was tuned such that the conductance was on the first conductance plateau, in order to minimize the Coulomb charge sensing effect. In the topmost line for weak coupling, ordinary Fano dips are observed. As

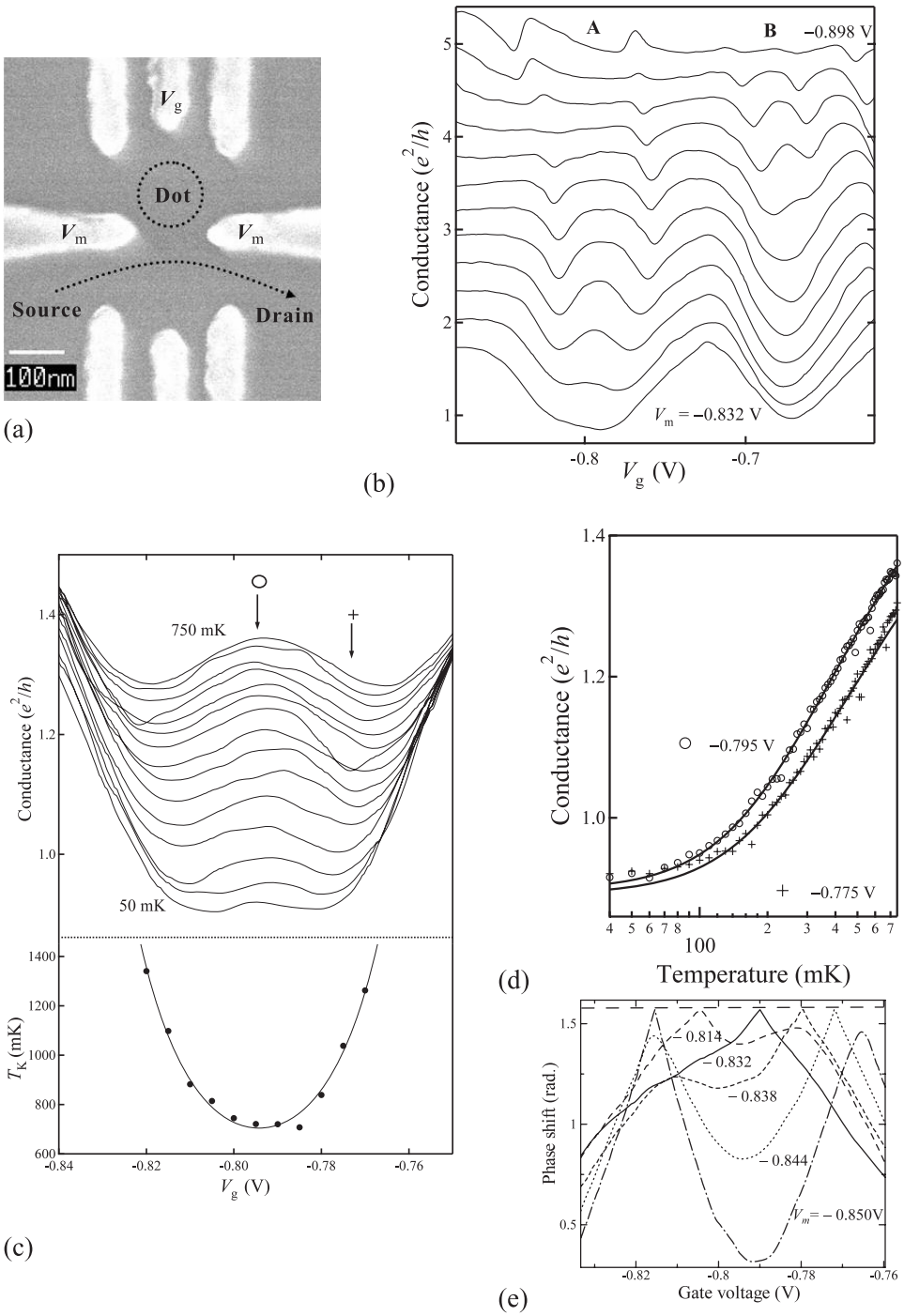

Figure 23. (a) Gate configuration of the sample. (b) Conductance of the wire measured at several coupling strengths tuned via V_m. The base temperature is 30 mK. The step in V_m is 6 mV and the data are offset by $0.3e^2/h$ for clarity. (c) Top: conductance as a function of gate voltage at temperatures from 750 to 50 mK with the temperature step of 50 mK. Bottom: Kondo temperatures T_K obtained from the temperature dependence. (d) Examples of the fitting to obtain T_K. (e) Phase shift of the QD obtained for the data at 50 mK for various coupling strengths. (From [59].)

the coupling strength increases, conductance between the dips (Coulomb valleys) decreases alternately, which leads to the merging of two neighbouring dips into one. This behaviour is very similar to that theoretically predicted for $q = 0$ (figure 22 (a)) and indicates the emergence of the FK effect. Here, with the increase of coupling strength, the Kondo temperature T_K increases, which means a decrease of effective temperature.

Figure 23(c) shows the temperature dependence of dip A, which is again very similar to figure 22(a). To be more quantitative, we focus on two gate positions indicated by ∘ and + and show their detailed temperature dependences in figure 23(d). In order to estimate T_K, we use an empirical formula for the temperature dependence $G(T)$ [60, 61]:

$$G(T) = G_0 - G_1\left(\frac{T_K'^2}{(T^2 + T_K'^2)}\right)^s, \tag{32}$$

where G_1, $T_K' \equiv T_K/\sqrt{2^{1/s} - 1}$ and s are fitting parameters. G_0 was fixed at $1.8e^2/h$, the wire conductance far from anti-resonance. Examples of the fitting are shown as lines in figure 23(d). The data below 120 mK were not included in the fitting because of electron temperature saturation. From the fitting, $s = 0.25 \pm 0.04$ was obtained, which is in accordance with the prediction for spin-1/2 impurities. The obtained T_K are plotted as a function of V_g in the lower panel of figure 23(c). T_K depends parabolically on V_g with the bottom around the midpoint of the Kondo valley, just as previously reported [62]. This dependence agrees well with the Kondo temperature,

$$T_K = \frac{\sqrt{\Gamma U}}{2}\exp\left(\frac{\pi\epsilon(\epsilon + U)}{\Gamma U}\right), \tag{33}$$

where Γ is the dot–wire coupling and ϵ is the single-electron level measured from the Fermi level. We obtained $U = 0.39 \pm 0.03$ meV and $\Gamma = 0.30 \pm 0.02$ meV by fitting the above function to T_K.

The phase shift of the Kondo state can be deduced by assuming the same scattering model as described in section 5.2 (figure 14(a)). Here, we can set $L = 0$, which corresponds to $q = 0$, for simpler analysis. On the other hand, because the reflection phase shift is measured in the present system, it is impossible to distinguish $\Delta\theta$ from $\pi/2 - \Delta\theta$, where $\Delta\theta$ is the phase shift of the transmission mode. Figure 23(e) displays the calculated transmission phase shift as a function of V_g for the FK lineshapes in figure 23(b) (dip A). The folding at $\pi/2$ is due to the reflection measurement. It is clear that $\Delta\theta$ approaches the curve for the locking to $\pi/2$ in the middle of the Coulomb valley.

8.3. The FK effect in an AB ring geometry

Ji and co-workers first reported phase measurements of QDs in the Kondo regime with open AB interferometers, in which multiple scattering was carefully avoided [63, 64], and hence no Fano effect appeared. Surprisingly, they found that the transmission phase shift did not show locking to $\pi/2$ and varied smoothly (almost linearly) through a Kondo peak even when the system was close to the unitary limit. The result raised strong doubt as to the applicability of the Anderson impurity model to QD systems, and hence an examination of phase locking in other systems is important.

In a two-terminal AB ring interferometer, transmission phase shift and reflection phase shift appear in a mixed manner, resulting in phase rigidity, as we demonstrated in section 2.1, which makes direct phase measurement difficult. However, this does not mean that phase shift locking cannot be observed in two-terminal devices. At a resonance point, that is, at the point of phase jump of primary AB oscillation with the period ϕ_0, the amplitude of the primary

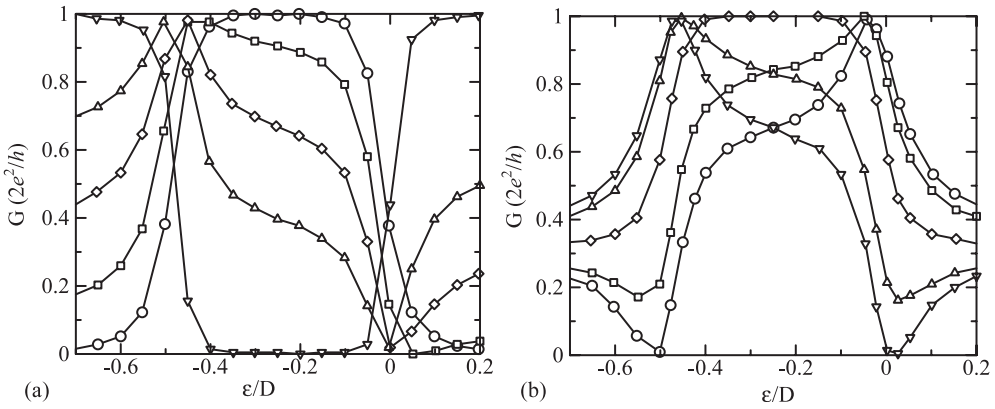

Figure 24. Calculated conductance of an AB interferometer with a quantum dot in the Kondo unitary limit as a function of the energy difference between the resonant level and the Fermi level. (a) Lineshape variation of conductance with dot-electrode coupling constant. (b) Magnetic flux evolution of the lineshape. Data taken from [22].

component diminishes to zero and those of higher harmonics increase. The same should occur, then, at Kondo resonances for a finite range of gate voltage. Such behaviour is predicted by a theory of the FK effect in a closed AB interferometer [22]. The results of that calculation are shown in figure 24.

In figure 24(a), FK lineshapes at a Coulomb valley are plotted for various coupling strengths. The value of q varies from infinite (a single peak) to finite (a peak + a shoulder + a dip) to zero (a single dip). A plateau or shoulder structure appears in the middle of the Coulomb valley due to phase shift locking. On the other hand, in figure 24(b), the coupling is fixed and the magnetic flux piercing the ring is varied by a half-flux quantum ($\phi_0/2$). With this change in the flux, e.g. at $\epsilon = 0$, the conductance changes from the peak to the dip, corresponding to a half-period of AB oscillation, while in the middle of the valley, the conductance recovers to the initial value (a full period). This is due to phase rigidity, which leads to the disappearance of the AB component with the period of ϕ_0. Consequently, frequency doubling occurs in the middle of the valley. Also, in this series of lineshapes, a plateau or a shoulder due to phase shift locking always appears in the middle.

Figure 25 shows our experimental results for the Fano–Kondo effect in a QD embedded in a two-terminal AB ring [65]. As shown in figure 25(a), a clear Kondo peak was observed in the total conductance. However, the AB component in the conductance is small in zero field and in order to observe sufficient amplitude, we should apply a magnetic field of about 0.5 T. To emphasize the response to the magnetic field, we extract the conductance that does not depend on the field or changes slowly with the field. Figure 25(b) shows the obtained AB oscillation component in grey scale as a function of the gate voltage and the magnetic field. Here, we have chosen a field area of two AB periods, though almost the same structure repeats for more than 20 periods in this field range. The black and white stripes, which express the AB oscillation, flow smoothly with gate voltage, reflecting the breaking of phase rigidity. The behaviour appears to be similar to that in the open AB interferometer [64], though a major difference lies in the FK lineshape. Figure 25(c) displays cross sections of the grey-scale plot along the four white broken lines in (b); these four curves correspond to a single cycle of the AB oscillation. A characteristic of these curves is that each has a plateau or a shoulder structure in the middle of the Coulomb valley.

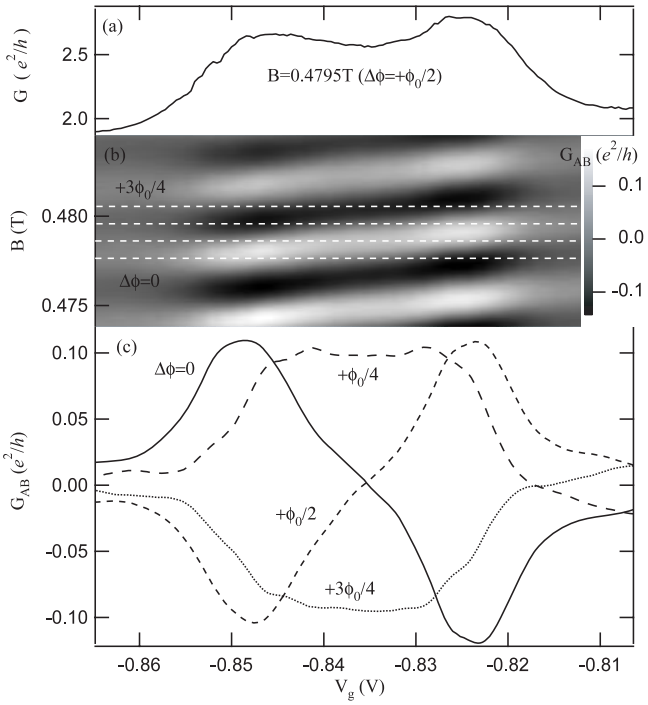

Figure 25. The Fano–Kondo effect in a QD embedded in an AB ring. (a) Total conductance of the ring around a Fano–Kondo peak. (b) Grey-scale plot of coherent conductance for 2.5 periods of AB oscillation. Each white broken line corresponds to a lineshape shown in (c). (c) Fano–Kondo lineshape and its response to the AB flux $\Delta\phi$ measured with flux quantum $\phi_0 \equiv h/e$ from $B = 0.47761$ T. Four representative lineshapes in a single AB cycle are depicted for $\Delta\phi = 0, \phi_0/4, \phi_0/2$, and $3\phi_0/4$. (From [65].)

Although the above result strongly suggests phase shift locking, the absence of frequency doubling, in other words the breaking of phase rigidity, must still be explained. A possible explanation is given using the theoretical model we adopted in section 4, in which the multichannel effect is considered. However, the model is not applicable to the present results, at least for many AB periods, because the model is designed to simulate the real physical situation with a multichannel interference circuit for a narrow field range, whereas the behaviour in figure 25 repeats over 20 AB periods. Also, particularly at the midpoint of a Coulomb valley, only the Kondo cloud state can carry the current, which means that, within the framework of the model, only the single loop associated with the Kondo cloud is effective for the conductance and phase rigidity cannot be broken.

Here, we apply the multichannel concept to elucidate a realistic physical mechanism of breaking phase rigidity [65]. At around 0.5 T, the magnetic length is about 35 nm, which is shorter than half the effective width of the arms, and the cyclotron radius is about 0.5 μm, which is comparable to that of the ring. This means the edge state is beginning to be formed but is not well defined. In order to take this situation into account we consider the conduction channels illustrated in figure 26 as a minimal model. Channel 1 is formed around the inner side of the AB ring by the magnetic field, which connects the left and right leads through the reference arm by $We^{i\varphi}$, or via the QD by $V_L^{(1)}$, $V_R^{(1)}$. Channel 2 is formed on the outer side and connects to the QD by $V_L^{(2)}$, $V_R^{(2)}$. In the QD, we consider a single energy level, ε_0, measured from the Fermi energy in the leads.

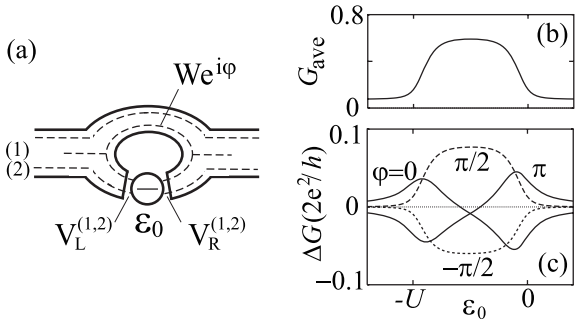

Figure 26. (a) Model of AB ring with two conduction channels, both of which couple to an energy level ε_0 in the embedded QD. Channel 1 is formed around the inner side of the AB ring, and is coupled to external electrodes (not shown) with probability p. (b) The conductance averaged over φ, $G_{\rm ave}$, and (c) $\Delta G = G(\varphi) - G_{\rm ave}$ as a function of ε_0. p is taken to be 0.5. The density of states in the leads is constant ν in the energy range of $[-D, D]$. $U = 0.5D$ and level broadening by $V_r^{(\alpha)}$ is $\Gamma_r^{(\alpha)} = 2\pi\nu V_r^{(\alpha)2} = 0.015D$ for all $\alpha = 1, 2$ and $r = L, R$. The transmission probability through the reference arm is $T_{\rm ref} = 4x/(1+x)^2 = 0.3$, where $x = (\pi\nu W)^2$. (From [65].)

In the Coulomb blockade region with an electron in the dot, $-U < \varepsilon_0 < 0$, the Kondo effect takes place and the Kondo cloud is formed with both channels 1 and 2. Electrons in channel 1 are resonantly transported through the Kondo cloud, whereas the coupling to channel 2 breaks the phase rigidity. We adopt the finite-U slave boson mean-field theory [66] to calculate the transport at $T = 0$. In figure 26(b), we show the conductance as a function of the dot level ε_0. In figures 26(b) and (c), we show the conductance as a function of the dot level ε_0, with a fixed phenomenological parameter $p = 0.5$. The conductance is enhanced by the Kondo effect and changes smoothly with φ, in good accordance with the experimental data shown in figure 25(c). The lineshape is periodic with the primary AB period. The above discussion presents a possible explanation for the present results and presumably covers the essential points. Thus the phase shift locking to $\pi/2$ in the middle of the Coulomb valley is now unquestionable.

We have reached the important conclusion that there should be an essential difference between closed interferometers and open ones other than those explainable within the Landauer–Büttiker scattering formalism. Then the origin of such a difference is naturally the next question, though we have no clear answer to this at present. In a closed interferometer, the wavefunction surrounding a QD is partly a standing wave, which emphasizes the nature of localization. This is similar for a Kondo cloud, and this common characteristic may facilitate collaboration between the two kinds of resonances and enable the Anderson impurity model to be applicable, though this is a naive qualitative inference.

Apart from the above problem an important difference between closed and open interferometers is the 'reaction' from the interference circuits to the Kondo effect. The theories so far introduced treat the unitary limit, i.e. $T = 0$. Interference or resonance in a system surrounding a QD affects the amplitude of the wavefunction at the junctions to the QD and thus the coupling strength Γ. Even within approaches based on the Anderson impurity model, this leads to the modification of $T_{\rm K}$ with the AB period in the case of an AB interferometer.

A phenomenon essentially the same as that above was observed in a QD with a ring structure. Modulation of the Kondo effect was clearly reflected in the magnetic-field variation of the current–voltage characteristics shown in figure 27(a). The height of the zero-bias anomaly ΔK showed peaks with the interval of AB oscillation (figure 27(b)). Figures 27(c)–(e) suggest that the modulation of ΔK (thus $T_{\rm K}$) is mainly due to that of Γ.

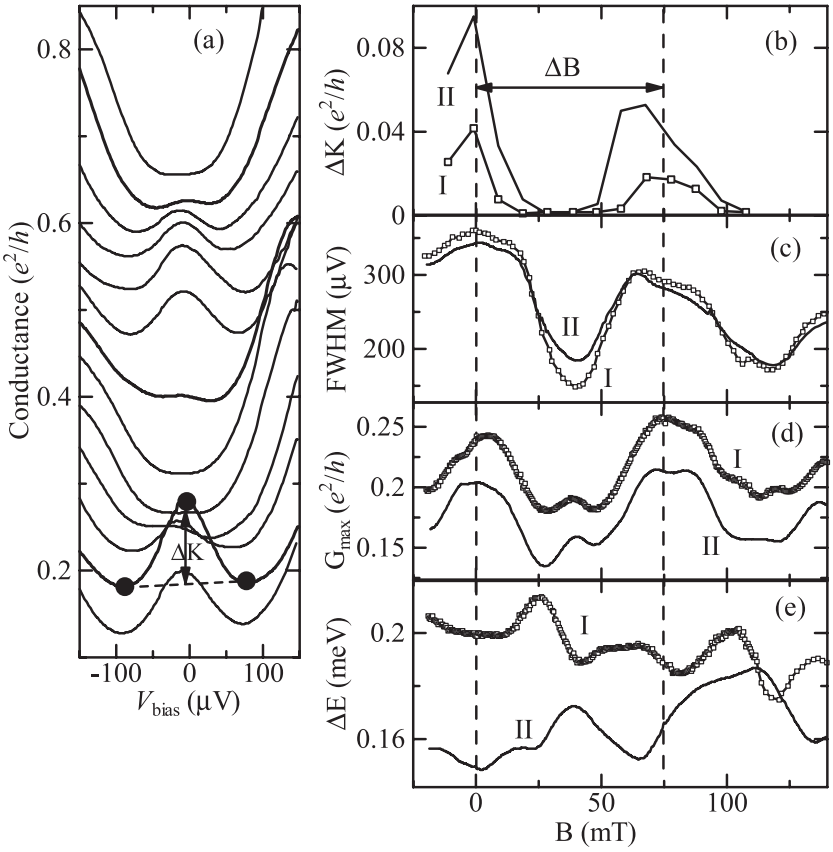

Figure 27. (a) Current–voltage characteristics of a quantum ring in the Kondo regime for different magnetic fluxes. The data are shifted by $0.1e^2/h$ for about $0.15\phi_0$. Zero-bias anomalies (amplitude ΔK) characteristic of the Kondo effect are strongly modulated with the magnetic field. (b) ΔK, (c) width of the zero-bias conductance (Kondo) peak (full width at half maximum, FWHM), (d) conductance peak height and (e) energy separation of single-electron levels ΔE plotted as a function of magnetic field B. ΔB is the AB period and I and II indicate two difference Coulomb diamonds. From [67].

Also in the case of a Kondo QD and an AB ring, similar modulation should exist and cause characteristic distortion of the AB oscillation, resulting in significant modification of the lineshape at finite temperatures [23, 68, 69]. Although this should cause the breakdown of the straightforward application of the Kondo theory at the unitary limit to closed interferometers, the applicability to open ones is unclear.

9. Summary

We have reviewed ‘phase shift measurements’ of quantum dots in two-terminal interference devices. The ‘phase rigidity’ problem has been overcome as a result of detailed analysis of the transmission through resonance, that is, the Fano effect. We have seen that the phase rigidity can be broken down by the multichannel effect. The existence of strongly coupled states has been proved, which should be a key to solving the problem of phase lapse. The creation of ‘partially coherent states’ has been observed to be a result of the reduction of the AB amplitude when spin scattering by a quantum dot exists, though the recovery of quantum coherence via

the growing of the Kondo cloud state has also been observed. Phase shift locking to $\pi/2$ has been observed in the Fano–Kondo effect in a T-shaped interferometer and an Aharonov–Bohm interferometer.

Acknowledgments

The author is grateful to K Kobayashi, H Aikawa, M Sato, A Sano, M Kitaji, T Otsuka, Y Hashimoto, A Endo and Y Iye for experimental collaborations, and to T Nakanishi, T Ando, M Eto, A Ueda, I Maruyama, K Ueda, K Kang, Y Avishai, A Aharony, O Entin-Wohlman, J König and Y Gefen for theoretical advice.

The work by the author's group reported in this article is supported by a Grant-in-Aid for Scientific Research from the Japanese Ministry of Education, Culture, Sports, Science and Technology.

References

[1] Tarucha S 1998 *Mesoscopic Physics and Electronics* (Berlin: Springer) p 66
[2] Kouwenhoven L P, Marcus C M, McEuen P L, Tarucha S, Westervelt R M and Wingreen N S 1997 *Proc. Advanced Study Institute on Mesoscopic Electron Transport* (Dordrecht: Kluwer) p 105
[3] Büttiker M 1988 *IBM J. Res. Dev.* **32** 63
[4] Aharony A, Entin-Wohlman O and Imry Y 2003 *Turk. J. Phys.* **27** 299
[5] Hackenbroich G 2001 *Phys. Rep.* **343** 463
[6] Aharonov Y and Bohm D 1959 *Phys. Rev.* **115** 485
[7] Berry M 1984 *Proc. R. Soc.* A **392** 45
[8] Onsager L 1931 *Phys. Rev.* **37** 405
[9] Aharony A, Entin-Wohlman O and Imry Y 2003 *Phys. Rev. Lett.* **90** 156802
[10] Kouwenhoven L P, van der Vaart N C, Nazarov Y V, Jauhar S, Dixon D, McCormick K, Orenstein J, McEuen P L, Nagamune Y, Motohisa J and Sakaki H 1996 *Surf. Sci.* **361/362** 591
[11] Fuhrer A, Löcher S, Ihn T, Heinzel T, Ensslin K, Wegscheider W and Bichler M 2001 *Nature* **413** 822
[12] Breit G and Wigner W 1936 *Phys. Rev.* **49** 519
[13] Schuster R, Buks E, Heiblum M, Mahalu D, Umansky V and Shtrikman H 1997 *Nature* **385** 417
[14] Yeyati A L and Büttiker M 1995 *Phys. Rev.* B **52** 14360
[15] Yacoby A, Heiblum M, Mahalu D and Shtrikman H 1995 *Phys. Rev. Lett.* **74** 4047
[16] Yacoby A, Schuster R and Heiblum M 1996 *Phys. Rev.* B **53** 9583
[17] Entin-Wohlman O, Aharony A, Imry Y and Levinson Y 2002 *J. Low Temp. Phys.* **126** 1251
[18] Fano U 1961 *Phys. Rev.* **124** 1866
[19] Aharony A, Entin-Wohlman O, Otsuka T, Katsumoto S, Aikawa H and Kobayashi K 2006 *Phys. Rev.* B **73** 195329
[20] Kobayashi K, Aikawa H, Katsumoto S and Iye Y 2002 *Phys. Rev. Lett.* **88** 256806
[21] Kobayashi K, Aikawa H, Katsumoto S and Iye Y 2003 *Phys. Rev.* B **68** 235304
[22] Hofstetter W, König J and Schoeller H 2001 *Phys. Rev. Lett.* **87** 156803
[23] Racec E R and Wulf U 2001 *Phys. Rev.* B **64** 115318
[24] Kim T-S, Cho S-Y, Kim C-K and Ryu C-M 2002 *Phys. Rev.* B **65** 245307
[25] Ueda A, Baba I, Suzuki K and Eto M 2003 *J. Phys. Soc. Japan* **72** (Suppl. A) 157
[26] Katsumoto S, Kobayashi K, Aikawa H and Iye Y 2003 *Superlatt. Microstruct.* **34** 151
[27] Kobayashi K, Aikawa H, Sano A, Katsumoto S and Iye Y 2004 *Phys. Rev.* B **70** 35319
[28] Johnson A C, Marcus C M, Hanson M P and Gossard A C 2004 *Phys. Rev. Lett.* **93** 106803
[29] Mohanty P and Webb R A 2000 *Phys. Rev. Lett.* **84** 4481
[30] Otsuka T, Katsumoto S, Iye Y and Kang K 2007 *J. Phys. Soc. Japan* (*Preprint* cond-mat/0701023)
[31] Gefen Y 2002 *Strongly Correlated Fermions and Bosons in Low-Dimensional Disordered Systems* (Dodrecht: Kluwer) p 13 (*Preprint* cond-mat/0207440)
[32] Yeyati A L and Büttiker M 2000 *Phys. Rev.* B **62** 7307
[33] Silvestrov P G and Imry Y 2000 *Phys. Rev. Lett.* **85** 2565
[34] Nakanishi T, Terakura K and Ando T 2004 *Phys. Rev.* B **69** 115307
[35] Baltin R, Gefen Y, Hackenbroich G and Weidenmüller H A 1999 *Eur. Phys. J.* B **10** 119

[36] Baltin R and Gefen Y 1999 *Phys. Rev. Lett.* **83** 5094
[37] Golosov D I and Gefen Y 2006 *Preprint* cond-mat/061342
[38] Göres J, Goldhaber-Gordon D, Heemeyer S, Kastner M A, Strikman H, Mahalu D and Meirev U 2000 *Phys. Rev.* B **62** 2188
[39] Zacharia I G, Goldhaber-Gordon D, Granger G, Kastner M A, Khavin Y B, Shtrikman H, Mahalu D and Meirav U 2001 *Phys. Rev.* B **64** 155311
[40] Aikawa H, Kobayashi K, Sano A, Katsumoto S and Iye Y 2004 *J. Phys. Soc. Japan* **73** 3235
[41] Werner S A, Colella R, Overhauser A W and Eagen C F 1975 *Phys. Rev. Lett.* **35** 1053
[42] Rauch H, Zeilinger A, Badurek G, Wilfing A, Bauspiess W and Bonse U 1975 *Phys. Lett.* **54A** 425
[43] Legget A 1992 *Quantum Tunnelling in Condensed Media* (Amsterdam: Elsevier) p 1
[44] Buks E, Schuster R, Heiblum H, Mahalu D and Umansky V 1998 *Nature* **391** 871
[45] Lin J J and Bird J P 2002 *J. Phys.: Condens. Matter* **14** R501
[46] Akera H 1993 *Phys. Rev.* B **47** 6835
[47] Akera H 1999 *Phys. Rev.* B **59** 9802
[48] König J and Gefen Y 2001 *Phys. Rev. Lett.* **86** 3855
[49] König J and Gefen Y 2002 *Phys. Rev.* B **65** 045316
[50] Mehta M L 1967 *Random Matrices and Statistical Theory of Energy Levels* (New York: Academic)
[51] Patel S R, Cronenwett S M, Stewart D R, Huibers A G, Marcus C M, Duruöz C I, Harris J S Jr, Campman K and Gossard A C 1998 *Phys. Rev. Lett.* **80** 4522
[52] Lüscher S, Heinzel T, Ensslin K, Wegscheider W and Bichler M 2001 *Phys. Rev. Lett.* **86** 2118
[53] Lindemann S, Ihn T, Heinzel T, Zwerger W, Ensslin K, Maranowski K and Gossard A C 2002 *Phys. Rev.* B **66** 195314
[54] Aikawa H, Kobayashi K, Katsumoto S and Iye Y 2004 *Phys. Rev. Lett.* **92** 176802
[55] Kondo J 1969 *Solid State Phys.* **23** 13
[56] Pustilnik M and Glazman L 2004 *J. Phys.: Condens. Matter* **16** R513
[57] Yoshimori A 1968 *Phys. Rev.* **168** 493
[58] Maruyama I, Shibata N and Ueda K 2004 *J. Phys. Soc. Japan* **73** 3239
[59] Sato M, Aikawa S, Kobayashi K, Katsumoto S and Iye Y 2005 *Phys. Rev. Lett.* **95** 066801
[60] Costi T A, Hewson A C and Zlatic V 1994 *J. Phys.: Condens. Matter* **6** 2519
[61] Goldhaber-Gordon D, Göres J, Kastner M A, Shtrikman H, Mahalu D and Meirav U 1998 *Phys. Rev. Lett.* **81** 5225
[62] van der Wiel W G, De Franceschi S, Fujisawa T, Elzerman J M, Tarucha S and Kouwenhoven L P 2000 *Science* **289** 2105
[63] Ji Y, Heiblum M, Sprinzak D, Mahalu D and Shtrikman H 2000 *Science* **290** 779
[64] Ji Y, Heiblum M and Shtrikman H 2002 *Phys. Rev. Lett.* **88** 076601
[65] Aikawa H, Katsumoto S, Iye Y and Eto M 2007 *Phys. Rev. Lett.* submitted
[66] Kotliar G and Ruckenstein A E 1986 *Phys. Rev. Lett.* **57** 1362
[67] Sigrist M, Fuhrer A, Ihn T, Ensslin K, Ulloa S E, Wegscheider W and Bichler M 2004 *Phys. Rev. Lett.* **93** 066802
[68] Aharony A and Entin-Wohlman O 2005 *Phys. Rev.* B **72** 073311
[69] Simon P, Entin-Wohlman O and Aharony A 2005 *Phys. Rev.* B **72** 245313